

*Emergence of self–organization of
atmospheric moist convection, as seen
through the energy–cycle in wavelet space*

Article

Published Version

Creative Commons: Attribution 4.0 (CC-BY)

Open Access

Yano, J.-I. and Plant, R. S. ORCID: <https://orcid.org/0000-0001-8808-0022> (2025) Emergence of self–organization of atmospheric moist convection, as seen through the energy–cycle in wavelet space. *Journal of Advances in Modeling Earth Systems*, 17 (4). e2024MS004517. ISSN 1942-2466 doi: 10.1029/2024MS004517 Available at <https://centaur.reading.ac.uk/120940/>

It is advisable to refer to the publisher’s version if you intend to cite from the work. See [Guidance on citing](#).

To link to this article DOI: <http://dx.doi.org/10.1029/2024MS004517>

Publisher: American Geophysical Union

All outputs in CentAUR are protected by Intellectual Property Rights law, including copyright law. Copyright and IPR is retained by the creators or other copyright holders. Terms and conditions for use of this material are defined in the [End User Agreement](#).

www.reading.ac.uk/centaur

CentAUR

Central Archive at the University of Reading

Reading's research outputs online



RESEARCH ARTICLE

10.1029/2024MS004517

Emergence of Self–Organization of Atmospheric Moist Convection, as Seen Through the Energy–Cycle in Wavelet Space

 Jun-Ichi Yano¹  and Robert S. Plant² 
¹CNRM (CNRS UMR3589), Météo France, Toulouse, France, ²Department of Meteorology, University of Reading, Reading, UK

Key Points:

- Both kinetic and available–potential energies tend to be transferred to larger scales as the convective organization is established
- At smaller scales, the generated available potential energy is immediately converted into kinetic energy, by following the free–ride balance under the weak temperature gradient approximation
- The kinetic energy generated by buoyancy from the available potential energy at small scales primarily manifests as gravity waves. The nonlinear horizontal self–advection of gravity waves is a principal process driving the cascade of kinetic energy from the smaller to larger scales

Correspondence to:

 J.-I. Yano,
jun-ichi.yano@cnr.fr

Citation:

 Yano, J.-I., & Plant, R. S. (2025). Emergence of self–organization of atmospheric moist convection, as seen through the energy–cycle in wavelet space. *Journal of Advances in Modeling Earth Systems*, 17, e2024MS004517. <https://doi.org/10.1029/2024MS004517>

Received 17 JUN 2024

Accepted 17 FEB 2025

Author Contributions:

Conceptualization: Jun-Ichi Yano, Robert S. Plant

Data curation: Jun-Ichi Yano

Formal analysis: Jun-Ichi Yano

Funding acquisition: Jun-Ichi Yano

Investigation: Jun-Ichi Yano, Robert S. Plant

Methodology: Jun-Ichi Yano, Robert S. Plant

Resources: Jun-Ichi Yano

Software: Jun-Ichi Yano

Abstract The energy cycle of a convectively–organized system, as realized by a convective–scale idealized simulation, is analyzed in wavelet space. In the equilibrium state, most of the available potential energy that is generated by convective heating is immediately converted into kinetic energy by means of buoyancy forcing, consistent with the free–ride principle. In turn, most of the generated convective kinetic energy is manifest as gravity waves propagating away from convective centers. The kinetic energy of these small–scale gravity waves is transferred upscale by their own advective nonlinearities. Finally, a large–scale circulation generated by this “inverse cascade” drives the formation of an organized structure in the precipitation field.

Plain Language Summary The basic element of cloudy atmospheric convection is the cumulus convective tower, about ten-km deep but only few kilometers in horizontal extent. As global satellite images suggest, atmospheric convection is often organized on much larger horizontal scales, even over few thousand kilometers, stretching over a tropical ocean. This study analyzes an idealized simulation of atmospheric convective organization. The vigorous vertical motions generated by the unstable cumulus towers are not directly responsible for such an organization tendency. The kinetic energy associated with those vertical motions is not retained therein for long, but rapidly released into the surrounding environment as propagating waves. The interactions of those propagating waves then generate a domain–wide circulation that leads to organization of convection.

1. Introduction

Over the tropical oceans, convective clouds tend to be organized into large scales. Individual cumulus clouds are agglomerated on the mesoscale as squall lines and cloud clusters (cf., Houze, 2018; Houze & Betts, 1981). These mesoscale structures are further organized on larger scales, most symbolically as super clusters (Nakazawa, 1988), and more generally as diverse types of convectively coupled equatorial waves (cf., Wheeler & Kiladis, 1999). The planetary-scale Madden-Julian oscillations (Lin, 2022; Zhang, 2005) could be considered the manifestation of convective organization at the largest scale. Tropical cyclones (cf., Smith & Montgomery, 2023) should also be mentioned as another important category of convective organization.

A major thread of research efforts has been to explain convective organizations from the perspectives of large–scale dynamics. Under this approach, as emphasized by Ooyama (1982), variations of individual convective elements in vertical structure and spatial arrangements are treated in an implicit manner by means of parameterizations, and thus only their collective effects to induce instability on larger scales are considered. Charney and Eliassen (1964) termed such a collective effect of convection as conditional instability of the second kind (CISK), and demonstrated this concept by developing a simple model of a tropical cyclone. Subsequent proposals of alternative theories such as wave-CISK (Hayashi, 1970; Lindzen, 1974) and WISHE (wind-induced surface exchange: Emanuel, 1987; Neelin et al., 1987; Yano & Emanuel, 1991) may be considered as variants of the original concept of CISK within the general perspective here.

An alternative perspective is that atmospheric convective organization may be generated spontaneously from convective-scale dynamics within a horizontally homogeneous environment without the need for any external large-scale forcing (such as a large-scale vertical motion). This idea can be traced to Nakajima and Matsuno (1988), who also demonstrated this possibility with a simple cloud-resolving model simulation. The same idea was further pursued by Yano et al. (1995, 1996) in simulations of a shallow-water analogue atmosphere

Supervision: Robert S. Plant
Validation: Jun-Ichi Yano
Visualization: Jun-Ichi Yano
Writing – original draft: Jun-Ichi Yano, Robert S. Plant
Writing – review & editing: Jun-Ichi Yano, Robert S. Plant

model with a simple representation of cumulus convection: see also a review by Yano (1998). This idea finally drew wider attention through a large-domain cloud-resolving simulation studied by Bretherton et al. (2005), who termed such a spontaneous generation of convective organization “self-aggregation” following the terminology introduced by Su et al. (2000).

The present study further pursues the idea of spontaneous generation of convective organization, or self-aggregation, through its own dynamics. The key idealizations in such a simulation are to assume a horizontally homogeneous environment with no rotation, typically characterized by a constant sea surface temperature (SST), and with a time-independent solar forcing, in line with earlier studies. We should of course recognize the pioneering nature of studies in two dimensions by Nakajima and Matsuno (1988) and Held et al. (1993), but we must also recognize that a different geometrical configuration qualitatively changes the nature of the dynamics (cf., Tennekes, 1978). It has been found that simulations over narrow channels with or without side walls (e.g., Tompkins, 2001a) somehow behave similarly to two-dimensional configurations, presumably due to fewer degrees of freedom in the channel-width direction. The present study focuses on the analysis of a three-dimensional simulation in a square horizontal domain.

The study addresses the mechanisms for the generation and maintenance of the self-aggregation form of convective organization. In the literature, this question has mainly been pursued by identifying feedback processes that enhance the tendency toward organized convection, as reviewed by Holloway et al. (2017), Wing et al. (2017), Wing (2019), and Muller et al. (2022).

The present study takes a different perspective, and addresses the same question from the point of view of the energy cycle between available potential energy (APE, or potential energy in short in the following) and the kinetic energy (KE) of the system. APE, as originally introduced by Lorenz (1955), can be used to construct an energy cycle of the global atmospheric circulation in combination with the kinetic energy by separating both into a zonal average and residual components (Oort, 1964; Oort & Peixoto, 1974). Both energy components can further be decomposed in the longitudinal wavenumbers (Saltzman, 1957, 1958).

To capture spatially localized features of the flow and the buoyancy field, which are reflected in the energy-density distributions, the energy cycle is here analyzed in wavelet space. Wavelet basis functions are known to be able to capture spatially localized features efficiently (e.g., Yano & Jakubiak, 2016; Yano, Moncrieff, Wu, & Yamada, 2001; Yano, Moncrieff, & Wu, 2001). The energy cycle in wavelet space can be considered a natural extension of the Fourier-space description by Salzmann (1958), Meneveau (1991), and Fournier (2002, 2003, 2005) previously performed energy-cycle analyses in wavelet space for fluid and atmospheric systems. A preliminary, yet complete description of the energy cycle in wavelet space, by extending the kinetic energy formulation by Fournier (2002), is considered by Yano (2003) for a study of the Madden-Julian oscillation. The present study further extends the treatment to a nonhydrostatic system.

A possible difficulty of proceeding in this manner is the definition of convective organization in terms of the energy cycle seen in wavelet space. Here, we will adopt a tentative definition of identifying large-scale organization with a concentration of energy at the lowest wavenumbers of the system. Such a definition is both practical and appropriate for the given context of an idealized simulation in a horizontally homogeneous environment. Thus, the question of the generation and maintenance of convective organization reduces to that of identifying the processes that transfer energy to and maintain energy at the lowest wavenumbers. A more specific question to be asked along this line is whether an energy peak at the lowest wavenumbers is maintained as a direct consequence of condensative heating associated with cumulus clouds or whether it is due to a different process. The present study provides a direct answer to this question. The importance of nonlinearity in the dynamics emerges prominently from this energy-cycle perspective. A link of the “convective aggregation” problem to stratified turbulence (e.g., Kimura & Herring, 2012; Lilly, 1983; Lilly et al., 1998; Riley & Lindborg, 2008) is suggested as a result.

A more difficult question is to explain how organized fields of cloud and precipitation are maintained by a given atmospheric flow that is organized on a large scale. Unfortunately, this question cannot be directly addressed in terms of the energy cycle between the available potential energy and the kinetic energy, and is thus left for a future, separate investigation. Nevertheless, we believe that the present study makes a first crucial step toward this ultimate goal, because it is most likely that an organized large scale is a key process to maintain such an organized structure of clouds and precipitation. Thus, the present study focuses on the question of a spontaneous generation of a large-scale organized circulation.

Investigations of the energy cycle in atmospheric convective systems are hardly new. For example, Holloway et al. (2013) examine the generation term of the available–potential energy as well as the potential–energy conversion into kinetic energy in their explicit simulation of Madden–Julian oscillations by a semi–global channel configuration, albeit using low–pass filtered data. In the context of studies of self–organization processes of moist atmospheric convection, Yang (2018, 2019) focuses on the budget of available potential energy (APE) in association with the moisture–entrainment–convection feedback, while Lai and Waite (2023) present a budget analysis of the horizontal component of kinetic energy associated with convective aggregation. By following up these previous studies, the present study presents an analysis of a full energy cycle of a convective system associated with organization.

The remainder of this paper is structured as follows. Section 2 describes the simulation studied and its evolution toward a state of large-scale organization. The wavelet decomposition is explained in Section 3, and the energy budget in wavelet space is set out in Section 4. Results are presented in Sections 5–7, in terms of the wavelet analysis of the system, the energy cycle, and a further decomposition of the system into buoyant and nonbuoyant components of the energy cycle following a similar wavelet–based approach. Section 8 considers the role of cold pools, and a final discussion is given in Section 9.

2. Emergence of Convective Organization

We adopt the standard simulation case by Holloway and Woolnough (2016), which assumes a tropical environment over a constant sea surface temperature (SST) with a solar forcing that is fixed in time, but otherwise with full radiation processes including cloud–radiation interactions. No Coriolis force is considered. Full details of the simulation can be found in the original paper, but a brief summary is provided in Section 2.1 for the sake of making this paper self–contained. The evolution of the precipitation field is presented in Section 2.2, which provides a good overview of the simulation case.

2.1. Simulation Case

An idealized simulation of a spontaneous generation of organized convection was performed with the Met Office Unified Model (Davies et al., 2005) on a doubly–periodic domain with sides of length 576 km in the horizontal and a horizontal grid spacing of 4 km. Hence, there are 144 grid points in each horizontal direction. There are 70 levels in the vertical with finer resolution used in the lower levels. The model top is at 40 km, with a sponge layer in the upper levels to absorb gravity waves. To avoid the effect of the sponge layer, but also to focus on the convective organization formed through the troposphere, the following analysis will be limited to the lowest 12 km. The number of vertical levels in the lowest 12 km is 56 with the vertical spacing stretching from 10 m at the surface to 690 m at the tropopause level.

Settings of the physics include Wilson and Ballard (1999) microphysics and 3D turbulent mixing through a Smagorinsky–Lilly approach (Lilly, 1962; Smagorinsky, 1963). The Gregory and Rowntree (1990) convection parameterization is also used, but with a closure time–scale that depends strongly on CAPE such that almost all precipitation is generated by explicitly–simulated convection (Holloway et al., 2013; Lean et al., 2008).

For the purpose of performing the wavelet analysis (cf., Section 3.1), the outputs with 144×144 horizontal points at each vertical level are interpolated into 128×128 points. As a result, the maximum wavenumber available in the data becomes 64, corresponding to a wavelength of 9 km. Three dimensional data is available every hour over the 40 days of the simulation, and surface precipitation is available every 15 min.

2.2. Evolution of the Precipitation Field

The tendency of the simulated convection to organize into a single coherent structure can relatively easily be identified, phenomenologically, by examining the evolution of the precipitation field in Figure 1. Holloway and Woolnough (2016) also present further corroborating metrics (e.g., spatial variance of total column water vapor).

Initial formation of a single dominant coherent structure is identified on day 8 (Figure 1d) as a consequence of gradually reducing the number of convective clusters, as seen over Figures 1a–1c. There is no indication found for systematic merging of the earlier convective clusters leading to a larger size when inspecting the precipitation field in animations with 15 min interval. Rather the convective clusters tend to be generated less frequently with time but with larger sizes and in close proximity to pre–existing clusters. However, this first dominant structure

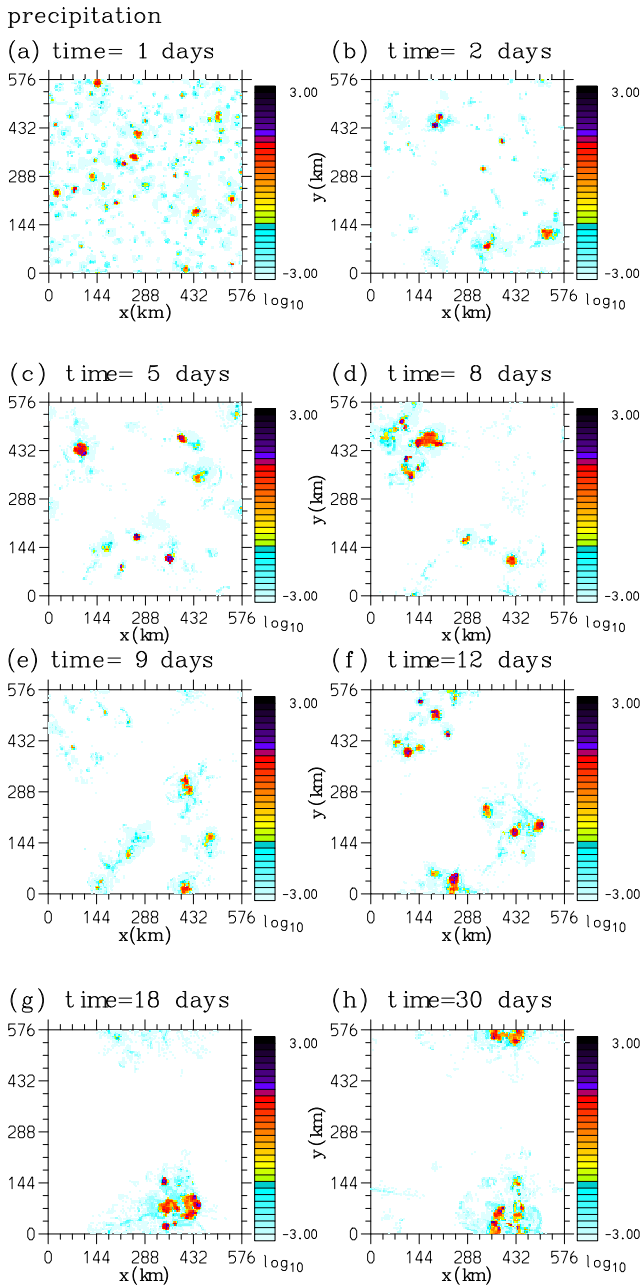


Figure 1. The evolution of the precipitation field: at $t = 1$ day (a), 2 days (b), 5 days (c), 8 days (d), 9 days (e), 12 days (f), 18 days (g), and 30 days (h). Shown in logarithmic scale over 10^{-3} to 10^3 mm/h.

decays within 24 hr (Figure 1e). A few days later the precipitation field becomes re-clustered (Figure 1f), and a well-organized single convective cluster emerges by day 18 (Figure 1g). This structure is sustained throughout the remainder of the simulation, as detailed in Holloway and Woolnough (2016), albeit with some intermittencies (cf., Figure 1h).

2.3. Basic Quantifications

The time series of domain-average precipitation is shown Figure 2. Aside from a strong spike exceeding 0.7 mm/hr in the initial 24 hr, the daily average does not change very strongly over the simulation period. In particular, there is no marked change in the average associated with the emergence of convective organization. A possible reflection of the organization is a gradual decrease of the dominant time scale for the precipitation fluctuations, noticeable after 15 days.

It might be anticipated that indications of convective organization may be better seen in higher-order statistics (cf., Cho & Polvani, 1996). However, time series of variance and skewness did not present any clear trend suggesting an increasing coherency with time (not shown).

3. Wavelet Decomposition Method

3.1. Preliminaries

The organization of the precipitation field in Figure 1 is more precisely characterized by its tendency to gradually cluster into a single area. Such spatially isolated structures are expected to be most efficiently represented using a wavelet approach (e.g., Yano & Jakubiak, 2016; Yano, Moncrieff, Wu, & Yamada, 2001; Yano, Moncrieff, & Wu, 2001). We adopt the Meyer wavelet (Meyer, 1992) for this purpose, taking advantage of its orthogonality and completeness. We refer to Mallat (1998) for the basics of the wavelet, and to Yano, Bechtold, et al. (2004) for the choice of the wavelet. As remarked in the latter paper, we choose the Meyer wavelet based on its good localization and analytical smoothness.

Any orthogonal complete wavelet constitutes a discrete set, taking the form, say, $\{\psi_{ij}(x)\}$, characterized by two indices: an index, i , that characterizes its scale, and another index, j , that characterizes the localization. The first index, i , spans over $i = -1$ to i_{\max} , where i_{\max} is related to the total number N of data values by $N = 2^{i_{\max}+1}$. The first value of this index, $i = -1$, corresponds to the domain average mode (with corresponding wavenumber, $k = 0$), and the remaining modes represent wavenumbers $k = 2^i$. Thus,

$$k = \begin{cases} 0 & i = -1 \\ 2^i & i \geq 0 \end{cases} \quad (1)$$

There is only a single domain-averaged mode with $i = -1$, but corresponding to the mode with wavenumber $k = 2^i$, we consider k localized modes, so that the localization index j spans over $j = 1$ to k . It also follows that when applying a discrete wavelet description, the given data set must consist of a number of data points matching an integer power of two. It is this point that motivates us to interpolate the simulation data in the manner described in Section 2.1.

The two indices, i and j , can be combined into a single index, l , which spans $l = 1$ to N (cf., Equation 3.3 of Yano, Moncrieff, Wu, and Yamada (2001), so that the wavelet modes may be expressed as $\psi_l(x)$. We adopt this notation in the following.

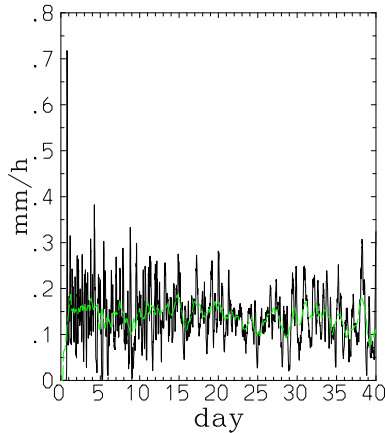


Figure 2. Time series of the domain-averaged hourly precipitation rate (solid) and a 1-day moving average (dashed green).

3.2. Two-Dimensional Extension

In the present study, we apply the wavelet decomposition on the horizontal plane of the system at each vertical level. For this purpose, the wavelet mode is extended into the two-dimensional case as $\psi_{l_x}(x)\psi_{l_y}(y)$ with the Equations 2–4 also generalized, in an analogous manner to the generalization of a Fourier transform into two dimensions. For ease of presentation, the following specific applications of the wavelet method will be presented for the one-dimensional case, with an obvious extension to the two-dimensional case assumed.

Keep in mind that as in the one-dimensional case, both l_x and l_y are defined as linear combinations of (i_x, j_x) and (i_y, j_y) , respectively. Also note that the wavenumbers k_x and k_y in these two directions are defined by

$$k_x = \begin{cases} 0 & i_x = -1 \\ 2^{i_x} & i_x \geq 0 \end{cases} \quad (5)$$

$$k_y = \begin{cases} 0 & i_y = -1 \\ 2^{i_y} & i_y \geq 0 \end{cases} \quad (6)$$

as a simple extension the one-dimensional definition (Equation 1).

3.3. Compression

The ability of wavelets to represent spatially-isolated, or pulse-like, structures efficiently can be exploited in several ways. First, a field that is dominated by pulse-like features can be represented well by a limited number of wavelet modes, truncating out the modes that do not contribute significantly. Such a representation can be called *compression*. The truncation level for the compression can be decided by a threshold, α , relative to the average variance, defined by

$$\varphi_c = \left(\frac{1}{N} \sum_{l=2}^N \tilde{\varphi}_l^2 \right)^{1/2} \quad (7)$$

excluding the domain average ($l = 1$) from the summation. As a result, a compressed set of wavelet coefficients, $\tilde{\varphi}_l^c$, is defined by

$$\tilde{\varphi}_l^c = \begin{cases} \tilde{\varphi}_l, & |\tilde{\varphi}_l| > \alpha\varphi_c \\ 0, & |\tilde{\varphi}_l| \leq \alpha\varphi_c \end{cases} \quad (8)$$

The discrete wavelets defined over the range, say, $[0, L]$ satisfy orthonormality defined by:

$$\frac{1}{L} \int_0^L \psi_{l'}(x)\psi_l(x)dx = \delta_{ll'} \quad (2)$$

where $\delta_{ll'}$ is Kronecker's delta. The orthonormality (Equation 2) enables the decomposition of any function, $\varphi(x)$, into wavelets as:

$$\varphi(x) = \sum_{l=1}^N \tilde{\varphi}_l \psi_l(x), \quad (3)$$

where the wavelet coefficients, $\tilde{\varphi}_l$ are defined by:

$$\tilde{\varphi}_l = \frac{1}{L} \int_0^L \varphi(x)\psi_l(x)dx. \quad (4)$$

for $l = 1, \dots, N$, and a compressed representation is given by:

$$\varphi^c(x) = \sum_{l=1}^N \tilde{\varphi}_l^c \psi_l(x). \quad (9)$$

In the following, only the standard case with $\alpha = 1$ will be considered.

The efficiency of such a compression can be quantified with two simple metrics. The first is the compression rate, defined by the ratio,

$$N_c/N, \quad (10)$$

of the number, N_c , of wavelet modes retained after compression Equation 8 to the total number of modes, N . The second is the fraction of the total variance that is represented after the compression, i.e., the explained fractional variance:

$$\sum_{l=2}^N \tilde{\varphi}_l^{c^2} / \sum_{l=2}^N \tilde{\varphi}_l^2. \quad (11)$$

3.4. Process-Based Decomposition

As an extension of the compression, we can decompose a variable, φ , into two components by examining whether a reference variable, say, χ , is dominant or not for a given wavelet mode. We may refer to the decomposition as providing high and low components of the variable φ , depending on whether the reference variable χ is dominant or not for the mode. Thus, the wavelet coefficients for the high and low components of φ are, respectively, set as:

$$\tilde{\varphi}_l^H = \begin{cases} \tilde{\varphi}_l, & |\tilde{\chi}_l| > \chi_c \\ 0, & |\tilde{\chi}_l| \leq \chi_c \end{cases} \quad (12)$$

$$\tilde{\varphi}_l^L = \begin{cases} 0, & |\tilde{\chi}_l| > \chi_c \\ \tilde{\varphi}_l, & |\tilde{\chi}_l| \leq \chi_c \end{cases} \quad (13)$$

where the split is based on the contribution of each mode to the variance of χ , thus:

$$\chi_c = \left(\frac{1}{N} \sum_{l=2}^N \tilde{\chi}_l^2 \right)^{1/2}. \quad (14)$$

Reconstructions of the high and low parts of the field φ are performed in the same manner as for Equation 9, but replacing the superscript, c , by H and L , respectively, for the high and low components.

It is straightforward to generalize this procedure to a set of variables, or a full physical system, by replacing φ with a vector. In this case, the whole system can be decomposed into the two components. For example, by adopting the horizontal wind shear as a reference variable, Yano, Moncrieff, and Wu (2001) decompose a full convective system into its mesoscale and convective-scale components without using either a scale dependent or threshold dependent criterion.

The process-based decomposition is the main methodology that is going to be extensively exploited in the present study. Here, note that formally, the same procedure can equally be applicable to any orthogonal decompositions, such as Fourier. However, only its combination with the wavelet enables us to extract spatially isolated features associated with a given process efficiently against the other features. Application of the same method to the Fourier decompositions would simply fail to obtain the same result.

3.5. Pulse Extraction

A further application is to extract a single pulse-like structure from a full system. The procedure is rather involved, and we refer to Appendix A of Yano, Blender, et al. (2004) for a full description. In short, we identify an extremum of the wavelet coefficient in the wavelet space spanning the two indices i (or equivalently the wavenumber k) and j , that represents a signature of a pulse-like structure of interest. We then identify a set, \mathcal{P} , of wavelet modes clustered around this extremum. As a result, the pulse-like structure, φ_p , is extracted as:

$$\varphi_p(x) = \sum_{l \in \mathcal{P}} \tilde{\varphi}_l \psi_l(x). \quad (15)$$

The two-dimensional extension is also straightforward conceptually as outlined in Yano and Jakubiak (2016). We also refer to Yano, Moncrieff, and Wu (2001) and Yano and Jakubiak (2016), respectively, for examples of one-dimensional and two-dimensional applications.

No doubt, the pulse extraction would be the most promising feature that can potentially be used to characterize the convective organizations. Yet, in the present study, we merely use this method for basic characterizations of the precipitation field (cf., Figure 4), but not in the energy-cycle analysis. The difficulty stems from that of identifying an appropriate reference variable to identify the pulse modes, as the subsequent discussions in Section 7.1 reveal.

4. Energy Cycle

4.1. System of Equations

To derive the energy cycle of the system, we start from the momentum equation in the form:

$$\frac{\partial \mathbf{v}}{\partial t} + \mathbf{v} \cdot \nabla \mathbf{v} = -c_{pd} \theta_v \nabla \pi' + \frac{\theta_v'}{\theta_v} \mathbf{g} + \mathbf{S}^v, \quad (16)$$

or alternatively,

$$\frac{\partial}{\partial t} \rho \mathbf{v} + \nabla \cdot \rho \mathbf{v} \mathbf{v} = -\rho c_{pd} \theta_v \nabla \pi' + \frac{\rho \theta_v'}{\theta_v} \mathbf{g} + \rho \mathbf{S}^v, \quad (17)$$

where

$$\nabla \cdot \rho \mathbf{v} \mathbf{v} = \rho(\mathbf{v} \cdot \nabla) \mathbf{v} + \mathbf{v}(\nabla \cdot \rho \mathbf{v}).$$

The notations are standard, and most importantly, \mathbf{v} is the three-dimensional velocity; \mathbf{S}^v represents dissipation terms, which is based a Smagorinsky-type subgrid mixing in this particular simulation (Holloway & Woolnough, 2016).

For defining the available potential energy (APE), we consider the virtual potential temperature perturbation, θ_v' , as a measure of the buoyancy of the system. Its governing equation is:

$$\frac{\partial \theta_v'}{\partial t} + \mathbf{v} \cdot \nabla \theta_v' + w \frac{d\bar{\theta}_v}{dz} = S^{\theta_v} \quad (18)$$

or alternatively,

$$\frac{\partial}{\partial t} \rho \theta_v' + \nabla \cdot \rho \theta_v' \mathbf{v} + \rho w \frac{d\bar{\theta}_v}{dz} = \rho S^{\theta_v}, \quad (19)$$

where

$$S^{\theta_v} = \frac{1 + q_v/\epsilon}{1 + q_T} S^{\theta} + \frac{\theta}{\epsilon(1 + q_T)} S^{q_v} - \frac{\theta_v}{(1 + q_T)^2} S^{q_T} \quad (20)$$

is the total source term for the virtual potential temperature, which is defined in terms of the source terms, S , for the potential temperature, θ , the water–vapor mixing ratio, q_v , and the mixing ratio, q_T , for the total water, as presented above with superscripts denoting the variables in concern. Recall the definition, $\epsilon = R_d/R_v$, of the ratio of gas constants for dry air to water vapor. The main contribution to the source, S^{θ_v} , for the virtual potential temperature is the diabatic heating, arising from the first term in Equation 20, but cloud physical processes that convert the water from one type to another also contribute through S^{q_v} and S^{q_T} .

Furthermore, mass continuity is given by:

$$\frac{\partial \rho}{\partial t} + \nabla \cdot \rho \mathbf{v} = 0, \quad (21)$$

where ρ is the dry–air density.

Also introduced is $\pi = (p/p_0)^{\kappa_d}$ the Exner function, where $\kappa_d = R_d/c_{pd}$ is the ratio of the dry ideal gas constant, R_d , to the specific heat, c_{pd} , of dry air at constant pressure. Furthermore, the potential temperature and the virtual potential temperature are, respectively, defined by:

$$\theta = \frac{T}{\pi},$$

$$\theta_v = \frac{1 + q_v/\epsilon}{1 + q_T} \theta.$$

Note further that some thermodynamic variables have been separated into mean and perturbation values by setting, for example, $\theta = \bar{\theta} + \theta'$, in which the mean, $\bar{\theta}$, is defined by a horizontal–domain average. This definition of the mean makes it time dependent. However, that is inconsequential in practice so long as the evolution of the mean state is sufficiently slow, as in the present simulation.

As a last minor technicality, we may note that the UM system assumes a fully compressible continuity equation, Equation 21, which explicitly includes sound waves. The energy cycle in the following is presented in a manner consistent with this fully compressible formulation, although the local change of density with time can be neglected in practice, and the contribution of the sound waves is insignificant in the simulation.

4.2. Energy Cycle in Physical Space

The energy cycle of the system in physical space can be obtained by multiplying the momentum, $\rho \mathbf{v}$, and the virtual potential–temperature perturbation, θ'_v , on the budget Equations 16 and 19 for the momentum and virtual potential–temperature, respectively. With the help of the continuity relation (Equation 21), and some renormalizations of the latter equation, we find:

$$\frac{\partial K}{\partial t} + \nabla \cdot (K + \rho c_{pd} \theta_v \pi') \mathbf{v} = C(P, K) + \rho \mathbf{v} \cdot \mathbf{S}^v + c_{pd} \pi' \left(\nabla \cdot \rho \theta'_v \mathbf{v} + \rho w \frac{d\bar{\theta}_v}{dz} \right), \quad (22)$$

$$\frac{1}{\sigma} \frac{\partial \sigma P}{\partial t} + \frac{1}{\sigma} \nabla \cdot \sigma P \mathbf{v} = -C(P, K) + \frac{\rho \theta'_v}{\sigma} S^{\theta_v}, \quad (23)$$

where the kinetic energy and the available potential energy (APE) are, respectively, defined by

$$K = \frac{\rho}{2} \mathbf{v}^2, \quad (24)$$

$$P = \frac{\rho}{2\sigma} \theta_v'^2. \quad (25)$$

Note that the available potential energy is normalized by dividing it by a stratification factor:

$$\sigma = \frac{\bar{\theta}_v}{g} \frac{d\bar{\theta}_v}{dz}. \quad (26)$$

In the following, the factor, σ , is treated as a constant with time, which was found to be a good approximation for the present simulation, and so the first term in Equation 23 can be considered the local tendency of APE. Importantly, potential energy is converted into kinetic energy with the rate:

$$C(P, K) = \rho g \frac{\theta'_v}{\bar{\theta}_v} w. \quad (27)$$

Although the present study does not examine the energy cycle in physical space explicitly, these expressions provide a good point of reference to understand the energy cycle in the wavelet space, which is presented next.

4.3. Energy Cycle in Wavelet Space

The energy cycle can also be considered within wavelet space in an analogous manner. For this purpose, the governing Equations 16–19 for the velocity and virtual potential–temperature, respectively, are first transformed into wavelet space by following the formula for the wavelet transform (Equation 4). The variables transformed into wavelet space will be marked by a tilde sign, as suggested by Equation 4. The energy cycle in wavelet space can be then derived by multiplying $\tilde{\rho}\tilde{\mathbf{v}}_l$ and $(\tilde{\rho}\tilde{\theta}_v)_l$, respectively, on the obtained governing equations for the velocity and virtual potential–temperature in wavelet space. In detail, a full derivation requires an extra step to account for the compressibility of the atmosphere (cf., Equation 21): the same procedure must also be repeated by multiplying $\tilde{\mathbf{v}}_l$ and $(\tilde{\theta}_v)_l$, respectively, on the governing equations for $\tilde{\rho}\tilde{\mathbf{v}}_l$ and $(\tilde{\rho}\tilde{\theta}_v)_l$. Taking the sums of these pairs of results leads to energy–budget equations. Here, the subscript, l , is adopted as a short-handed expression for a particular wavelet mode, which consists of two components under the two–dimensional space decomposition, thus, $l = (l_x, l_y)$.

The whole derivation is rather lengthy, and not reproduced here, but it is performed in analogous manner as the energy–cycle is derived in the Fourier space (cf., Saltzman, 1957). The final results are:

$$\frac{\partial}{\partial t} \tilde{K}_l - \tilde{N}_l(K) = \tilde{F}_l(K) + \tilde{C}_l(P, K) + \tilde{S}_l(K), \quad (28)$$

$$\frac{1}{\sigma} \frac{\partial}{\partial t} \tilde{P}_l - \tilde{N}_l(P) = -\tilde{C}_l(P, K) + \tilde{S}_l(P), \quad (29)$$

where the kinetic and potential energies are, respectively, defined by:

$$\tilde{K}_l = \frac{1}{2} (\tilde{\rho}\tilde{\mathbf{v}})_l \tilde{\mathbf{v}}_l, \quad (30)$$

$$\tilde{P}_l = \frac{1}{2\sigma} (\tilde{\rho}\tilde{\theta}'_v)_l \tilde{\theta}'_{v,l}. \quad (31)$$

Recall that the stratification factor, σ , is defined by Equation 26. The conversion rate from potential to kinetic energy is:

$$\tilde{C}_l(P, K) = \frac{g}{2\bar{\theta}_v} \left[(\tilde{\rho}\tilde{w})_l \tilde{\theta}'_{v,l} + \tilde{w}_l (\tilde{\rho}\tilde{\theta}'_v)_l \right]. \quad (32)$$

Nonlinear advection and pressure forcing terms are introduced by:

$$\tilde{N}_l = \tilde{N}_{l,H} + \tilde{N}_{l,V}, \quad (33)$$

$$\tilde{F}_l(K) = \tilde{F}_{l,H}(K) + \tilde{F}_{l,V}(K) \quad (34)$$

dividing them further into horizontal and vertical contributions, as designated by the subscripts, H and V , respectively. Here,

$$\tilde{N}_{l,H}(K) = -\frac{1}{2}[\langle \rho \tilde{\mathbf{v}} \rangle_l \cdot \langle \mathbf{u} \cdot \nabla_H \mathbf{v} \rangle_l + \langle \nabla_H \cdot \rho \mathbf{u} \mathbf{v} \rangle_l \cdot \tilde{\mathbf{v}}_l], \quad (35)$$

$$\tilde{N}_{l,V}(K) = -\frac{1}{2}[\langle \rho \mathbf{v} w \rangle_l \cdot \frac{\partial \tilde{\mathbf{v}}_l}{\partial z} + \tilde{\mathbf{v}}_l \cdot \left\langle \mathbf{v} \frac{\partial \rho w}{\partial z} \right\rangle_l], \quad (36)$$

$$\tilde{N}_{l,H}(P) = -\frac{1}{2\sigma}[\langle \mathbf{u} \cdot \nabla_H \theta'_v \rangle_l \cdot \langle \rho \theta'_v \rangle_l + \langle \nabla_H \cdot \rho \mathbf{u} \theta'_v \rangle_l \tilde{\theta}'_{vl}], \quad (37)$$

$$\tilde{N}_{l,V}(P) = -\frac{1}{2\sigma}[\langle \rho \theta'_v \rangle_l \left\langle w \frac{\partial \theta'_v}{\partial z} \right\rangle_l + \tilde{\theta}'_{vl} \left\langle \frac{\partial \rho w \theta'_v}{\partial z} \right\rangle_l], \quad (38)$$

$$\tilde{F}_{l,H}(K) = c_{pd} \tilde{\pi}'_l \langle \nabla_H \cdot \rho \mathbf{u} \theta'_v \rangle_l, \quad (39)$$

$$\tilde{F}_{l,V}(K) = -c_{pd} \langle \rho w \theta'_v \rangle_l \frac{\partial \tilde{\pi}'_l}{\partial z}, \quad (40)$$

and $\langle * \rangle_l$ designates the l -th wavelet component of the combination within angled brackets, i.e., the domain average integral of that combination multiplied by ψ_l (Equation 4).

Here, all those nonlinear terms (Equations 35–40) are defined solely in terms of projections of variables to the l -th mode. However keep in mind that by projecting nonlinear terms, e.g., $\mathbf{u} \cdot \nabla_H \mathbf{v}$ as a first example, to the l -th mode, they contain the contributions of other modes from both \mathbf{u} and \mathbf{v} . Thus, the nonlinear terms contribute to transferring energy from one mode to another in wavelet space. This fact would become particularly important in interpreting the results after decomposing the system into two components by the process-based decomposition introduced in Section 3.4, because after the decomposition, such terms also contribute to transfers of energy from one component to another.

However, we also need to note a drawback of the given formulation for nonlinear advection terms (Equations 35–38): since they are not explicitly presented in terms of inter-mode transfers, we cannot directly infer the direction of the energy transfer associated with a given term. Although an attempt was made, it turns out to be difficult to achieve this goal due to the lack of a simple expression under the wavelet decomposition, as against that found with the Fourier or the spherical harmonics (cf., Equation 12 of Augier & Lindborg, 2013). In the following, we infer the direction of the energy transfer (“cascade”) in wavelet space by examining the distribution of signs of the nonlinear terms within the wavelet space.

Also keep in mind that the vertical advection terms not only consist of inter-mode transfers, but also a more direct vertical transfer in the form of flux (cf., Augier & Lindborg, 2013). Although less obvious, the same issue also arises with the horizontal advection terms to a lesser extent, because to transform those terms into a horizontal flux form, the mass continuity must be invoked, and thus part of those terms turns into a vertical flux component. The formulation unfortunately does not distinguish those different contributions. In the following, this issue is partially circumvented by evaluating the energy-cycle budget as an average over the troposphere, and as a result, the flux crossing the tropopause is not a significant part of the budget, as verified later in Section 6.1.

We emphasize also, that by decomposing the physical fields into wavelets for the horizontal directions, we exclusively focus on the transfer of energies over different horizontal scales. To this process, both horizontal and vertical advection processes can contribute. However, the transfer of energy by vertical advection in this context only refers to transfers across horizontal scales, with no connotation of a vertical cascade intended.

Finally, the source terms, $\tilde{S}(K)$ and $\tilde{S}(P)$, are defined by

$$\tilde{S}_l(K) = \frac{1}{2}[\langle \rho \tilde{\mathbf{v}} \rangle_l \cdot \tilde{\mathbf{S}}_l^v + \tilde{\mathbf{v}}_l \cdot \langle \rho \tilde{\mathbf{S}}^v \rangle_l] \quad (41)$$

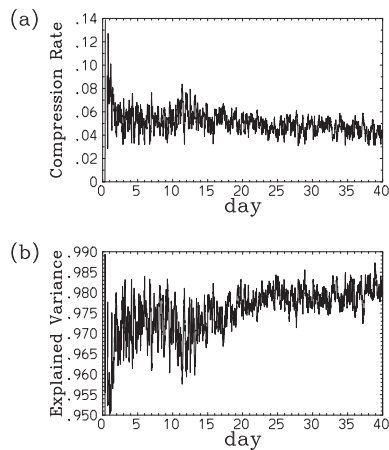


Figure 3. Time series of (a) the compression rate (Equation 7) and (b) the fractional explained variance after compression (Equation 8) for the precipitation.

$$\tilde{S}_l(P) = \frac{1}{2\sigma} \left[(\tilde{\rho}\tilde{\theta}^v)_l \tilde{S}_l^{\theta_v} + \tilde{\theta}^v_{vk} (\tilde{\rho}\tilde{S}^q)_l \right] \quad (42)$$

in terms of the source terms, \tilde{S}^v and \tilde{S}^{θ_v} , for the momentum and the virtual potential temperature.

The nonlinear advection terms (Equations 35–38) are the equivalents in wavelet space of the second terms on the left–hand sides of Equations 22 and 23, and the pressure terms (Equations 39 and 40) are equivalent to the last term on the right–hand side in Equation 22. In the following, the subscript, l , for a wavelet mode index will be omitted for economy of presentation.

4.4. Data Diagnosis Issues

The simulation of our interest can, in principle, be analyzed in wavelet space after transforming all of the required variables, following the formulation of the last subsection in a straightforward manner. However, we encounter some practical issues. First, the data have been stored only every hour without including the instantaneous tendencies as outputs. Hence, the local tendencies of the energies are estimated by taking a centered difference across output steps. All the other terms are evaluated as instantaneous values based on the

one-hourly outputs. Second, the full physical source terms, S , with various superscripts, have not been included as outputs, but only for selected physical processes. For this reason, the source terms, \tilde{S} , are diagnosed as residuals of the budgets. Note that the diagnosis can involve substantial errors at a given time due to the finite differencing. However, in the following, this issue is mostly circumvented by studying long time averages of the energy budget so that the local-in-time tendencies no longer contribute.

5. Basic Wavelet Analysis

In the present section, we present some basic analyses of the simulation in wavelet space before proceeding to the full energy cycle analysis in the next section.

5.1. Wavelet Compression

As explained in Section 3.3, the efficiency of a wavelet representation can conveniently be measured as the fractional number of modes retained by “compression” (the compression rate: Equation 10) and the fraction of the variance explained after the compression (Equation 11).

Figure 3 shows time series of these measures for the simulated precipitation, and demonstrates that the compression efficiency is high throughout. The compression rate decreases and the explained variance increases somewhat over time, although the changes are hardly dramatic, apart from some initial spin–ups over the first two days or so. The tendencies are temporarily reversed between c.a., 10–15 days corresponding to the de–integration of the initial convective organization and its gradual re–emergence, as described in Section 2.2. A similar indication for de–integration and re–emergence of organization is also found in the compression measures for the kinetic–energy time series (not shown), but not for the potential energy, or for the energy source and conversion terms.

5.2. Pulse Extraction

As shown by Yano, Blender, et al. (2004), and Yano and Jakubiak (2016), the wavelet approach can be useful to extract isolated features as a “pulse” (cf., Section 3.5). We have attempted such extractions for the precipitation field at individual times, without any consideration of the continuity in time. Thus, the identified “pulses” given in order of the decreasing explained fractional variances in the following, do not necessarily represent entities that are coherent in time. As it turns out, with the present system, this wavelet–based “pulse” extraction method does not extract an organized convective structure in a satisfactory manner, reflecting the fact that the precipitation features are not quite as isolated in wavelet space as they might appear from a visual inspection in physical space. For this reason, we decided not to pursue the idea of pulse extraction from the precipitation any more in the following.

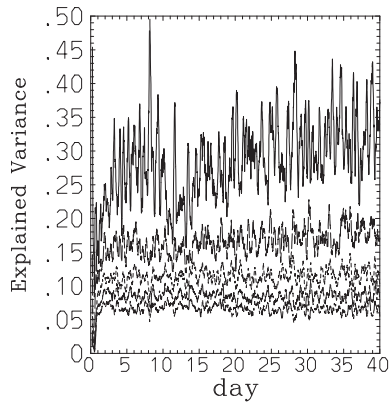


Figure 4. Time series of the explained-fraction of variances of the first five extracted pulse modes of precipitation, with varying types of curves. The series are presented as moving averages over 6 hr and the pulse modes are ordered by the explained fractions.

5.3. Evolution in Wavelet Spectrum Space

The tendency for the system to become organized onto larger scales is well captured within the wavenumber–spectrum space. Here, the spectra (or the mean spectrum, as it is called by Yano, Moncrieff, Wu, and Yamada (2001)) of the energies and the energy budget terms are constructed from the sum of all the contributions of wavelet modes for a given wavenumber scale, k , e.g.,

$$\tilde{K}(k_x, k_y) = \sum_{j_x=1}^{k_x} \sum_{j_y=1}^{k_y} \tilde{K}_l \Big|_{i_x, i_y} . \quad (43)$$

Here, the subscript after the vertical bar suggests that the sum is taken by fixing the value of i_x and i_y to those corresponding to the given wavenumbers k_x and k_y . Recall that $l = (l_x, l_y)$, and those indices l_x and l_y for the two coordinates can further be separated into the two indices i and j with the subscripts for the coordinates to be added. Also recall that the wavenumber spectra for the energy conversion terms introduced in Section 4.3 are also defined in an analogous manner as Equation 43, and will be discussed later in Sections 6 and 7.

On the other hand, a squared sum of wavelet coefficients is adopted for a direct wavelet decomposition of the precipitation, \tilde{R} , i.e.,

$$\tilde{R}(k_x, k_y) = \sum_{j_x=1}^{k_x} \sum_{j_y=1}^{k_y} \tilde{R}_l^2 \Big|_{i_x, i_y} . \quad (44)$$

Spectra for precipitation, kinetic and potential energies are presented in Figures 5, 6, and 9, respectively. Note that here and in the following, all of the energy–related variables are presented in terms of averages over the lowest 12 km, up to the simulated tropopause level, as obtained from integrals of geometrical height.

The precipitation spectrum presents the first clear peak after about 1 day of simulation (Figure 5a), following an initial precipitation burst, which dies out very quickly. However, it takes a few days for the power to develop (Figures 5b and 5c), and one needs to wait until day 7 to see its full development (Figure 5d). Unlike the energy spectra, we see little evidence of the power moving toward the lower wavenumbers with time.

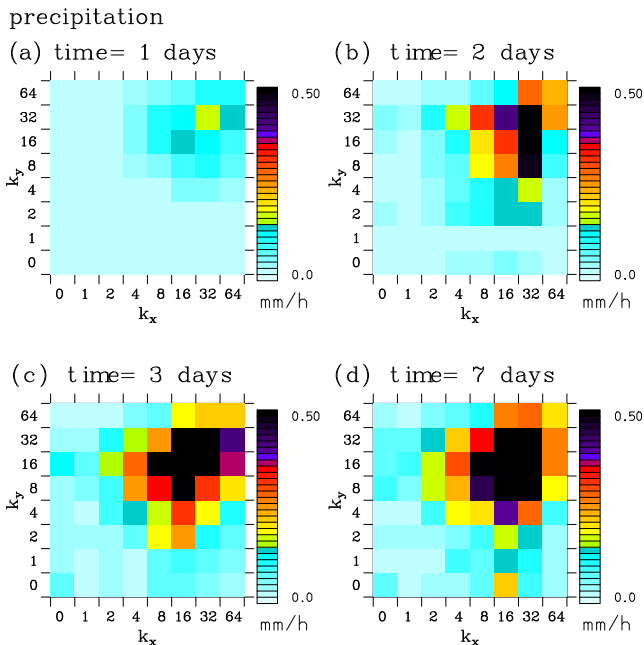


Figure 5. The power spectrum of precipitation at $t = 1$ day (a), 2 days (b), 3 days (c), and 7 days (d) with the wavenumbers, k_x and k_y , in two horizontal directions as axes. Here, the times shown are not identical to those in Figure 1, because the evolution of the spectrum does not perfectly correspond to that in physical space.

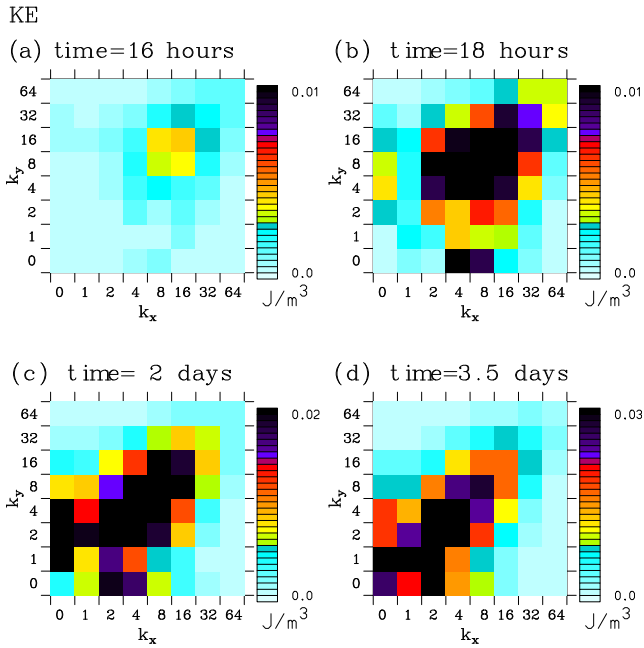


Figure 6. The kinetic–energy spectrum at $t = 16$ hr (a), 18 hr (b), 2 days (c), and 3.5 days (d).

The kinetic energy (KE) spectrum grows rapidly. Noticeable kinetic energy is already found at the wavenumbers, $k_x = k_y = 8$ and 16 after 16 hr (Figure 6a). As the kinetic energy grows further (Figure 6b), its spectral peak moves toward lower wavenumbers (Figure 6c). The process continues for 3–4 days before the kinetic–energy spectrum approaches an equilibrium (Figure 6d). The long–term evolution of the kinetic–energy spectrum is shown in Figure 7 for selected wavenumbers.

On the other hand, when only the vertical component of the kinetic energy is considered (Figure 8), its distribution evolves by closely following that of the precipitation spectrum (Figure 5). If the horizontal component of the divergent wind field is diagnosed from the vertical velocity, and its spectrum is plotted (not shown), we essentially recover the evolution of the distribution seen in Figure 6, reflecting the fact that the kinetic–energy spectrum, \tilde{K}_H , of the horizontal component is effectively recovered from the vertical counterpart, \tilde{K}_V , by $\tilde{K}_H = k^{-2} \tilde{K}_V$ in terms of the total wavenumber, $k = (k_x^2 + k_y^2)^{1/2}$. This analysis suggests that the overall circulation of this system is divergent, reflecting the fact that without the rotational effect, there is no effective process for generating a rotational flow.

The evolution of the potential energy spectrum (Figure 9) is slower than for the other two variables, and we need to wait for a day to notice significant values. The initial energy peaks are found at lower wavenumbers than for the kinetic energy, and higher values tend to be more spectrally dispersed. There are peaks at $(k_x, k_y) = (4, 2)$ and $(0, 4)$ at $t = 1$ day (Figure 9a). The accumulation of the spectrum at the lowest wavenumbers takes 2–4 days (Figures 9b and 9c). At the next stage, the potential energy power begins to decrease (Figure 9d), and this tendency continues for a further 10 days.

The next goal is to identify the processes leading to the transfer of energy to larger scales. For this purpose, we turn to the energy cycle of the system.

6. Wavelet–Space Energy-Cycle Analysis

6.1. Kinetic Energy (KE)

The kinetic energy budget averaged over the first 10 days ($t = 0$ –10 days) is shown in Figure 10. Note that after averaging longer than, say, 2 days, the budget is close to equilibrium, with the total gain well balanced with the total loss at a given wavenumber. In the following, the pressure term, $\tilde{F}(K)$, will not be shown, because this term does not contribute significantly: it remains at the level of 10^{-8} J/m³/s throughout the simulation. As a detail, $\tilde{F}_V(K)$ is consistently larger in magnitude than $\tilde{F}_H(K)$, although one might intuitively expect $\tilde{F}_H(K) + \tilde{F}_V(K) \simeq 0$. This reflects the fact that energy is systematically transported upwards to be absorbed in the sponge layer at the top, and the term $\tilde{F}_V(K)$ contributes to this process.

The kinetic energy, \tilde{K} , is generated by buoyancy from the potential energy, \tilde{P} , through the conversion term, \tilde{C} , (Figure 10a) over a wide range of scales, but more heavily at the high wavenumbers. This energy conversion term, \tilde{C} , is primarily balanced at each wavenumber through the loss term, $-\tilde{S}(K)$, (Figure 10b). Nevertheless, the gain is slightly larger over the wavenumbers of 8–32.

The remaining slight imbalance between the conversion and the sink, $\tilde{C} + \tilde{S}(K)$, thus indicates a local gain and loss at some wavenumbers. The close equilibrium is maintained by nonlinear transfer, $\tilde{N}(K)$ (cf., Equation 32),

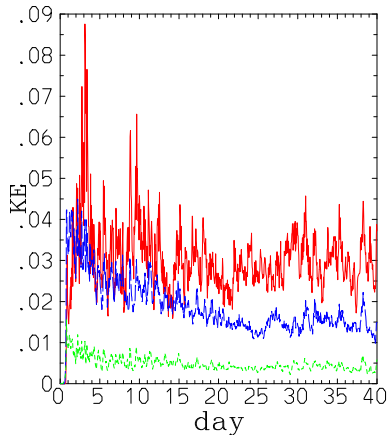


Figure 7. Time series of the kinetic–energy spectrum for selective wavenumbers: $k_x = k_y = 2$ (red), 8 (blue), 32 (green).

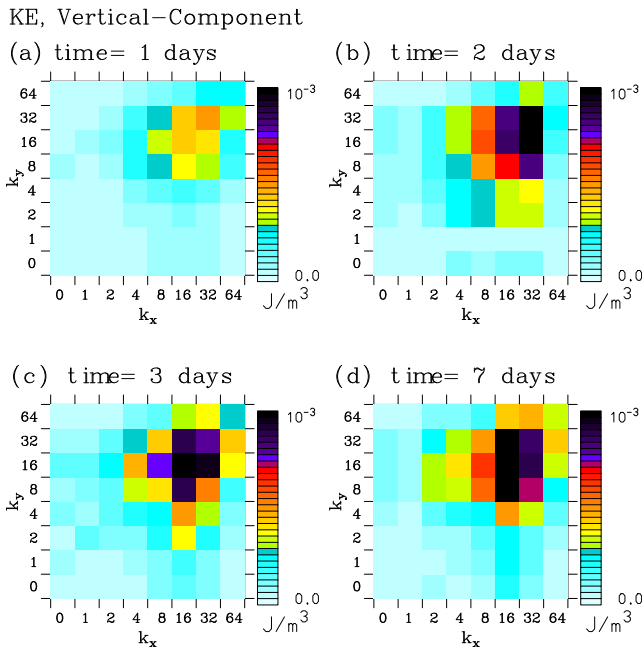


Figure 8. The spectrum for the vertical component of the kinetic energy at $t = 1$ day (a), 2 days (b), 3 days (c), and 7 days (d).

by advection. As seen in the lower row of Figure 10, the tendencies due to the horizontal, $\tilde{N}_H(K)$, (c) and vertical advection, $\tilde{N}_V(K)$, (d) are strikingly different: the vertical advection, $\tilde{N}_V(K)$, transfers the energy from the smallest scales ($k_x = 64$ or $k_y = 64$: with energy loss at this scale) to the larger scales, with the largest gain found at $k_x = k_y = 8$. On the other hand, the horizontal advection, $\tilde{N}_H(K)$, transfers energy from medium scales ($k_x = 16\text{--}32$ or $k_y = 16\text{--}32$) to both smaller and larger scales, with the largest gain occurring at larger scales over $k_x = 2\text{--}4$ and $k_y = 2\text{--}4$. It may be worthwhile to note that the medium wavenumber range roughly matches with the scales that dominate the spectral power of the precipitation field (cf., Figure 5).

The forward cascade by horizontal advection toward the smaller scales is substantially canceled out by the inverse cascade by vertical advection from the smaller scales. As a result, the nonlinear transfer of kinetic energy by advection, $\tilde{N}(K)$, is overall dominated by an inverse cascade: as whole, the kinetic energy is transferred from smaller scales ($k_x = 8\text{--}64$ or $k_y = 8\text{--}64$) to the larger scales. The forward part of the cascade by the horizontal component of advection is consistent with the finding by Lai and Waite (2023), focusing on the budget of the kinetic energy of the horizontal component. However, the inverse-cascade by horizontal advection from the medium scales to the larger scales was not present in their simulation

The reasons for a different cascade behavior between our results and those of Lai and Waite (2023) are not immediately clear. Two features of the simulation by Lai and Waite (2023) stand out: a relatively low model top at 25 km (with a relatively shallow sponge layer of 5 km depth), and a high resolution in the vertical (199 levels). The first feature has a risk of allowing some artificial reflections from the model top. On the other hand, the second feature helps to resolve stratified-turbulence eddies better than the present simulation (cf., Section 9.5.1). We may also note a difference in turbulent mixing (TKE closure vs. Smagorinsky).

A possible concern here is the potential significance of the vertical transfers of energy that are included both in the horizontal and vertical advection terms, $\tilde{N}_H(K)$ and $\tilde{N}_V(K)$. Their magnitude can be estimated by taking the sum of each advection spectrum, because the pure exchange of energy between horizontal modes would cancel out by taking the sum. The average sums of the \tilde{N}_H and \tilde{N}_V spectra are $-2.836 \times 10^{-9} \text{ J/m}^3/\text{s}$ and $2.809 \times 10^{-8} \text{ J/m}^3/\text{s}$, respectively. We have attempted a simple correction of the spectra to remove these averages from assuming that the vertical energy-flux spectrum is “white.” However, the averages are small enough to leave the advection spectra essentially unchanged. The assumption of a white spectrum of vertical fluxes is reasonable, considering that the transfer is expected to be predominantly upwards. This assumption, and the estimated magnitude of such vertical transfer effects, is also supported by examining the spectrum of $\langle \rho \mathbf{v} \mathbf{w} \rangle_l \cdot \tilde{\mathbf{v}}_l$.

The same properties of the tendencies as just discussed for the average over the first 10 days also hold over shorter time averages (down to two-day averages), albeit with a slightly narrower range for the medium wavenumbers ($k_x = 16\text{--}32$ or $k_y = 16\text{--}32$) during the first four days of simulation. In particular, the presence of the “inverse cascade” driven by horizontal advection is maintained throughout the simulation and with a similar imbalance between the conversion and the sink. A minor noticeable feature at later stages is that the medium range of scales over which kinetic energy is lost by nonlinear advection tends to expand toward the larger scales ($k_x = 4\text{--}32$ or $k_y = 4\text{--}32$; Figure 11).

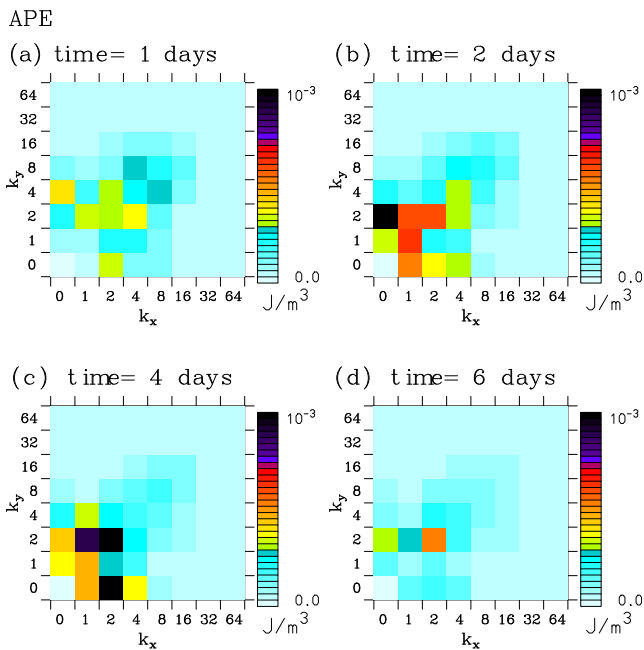


Figure 9. The potential energy spectrum at $t = 1$ day (a), 2 days (b), 4 days (c), and 6 days (d).

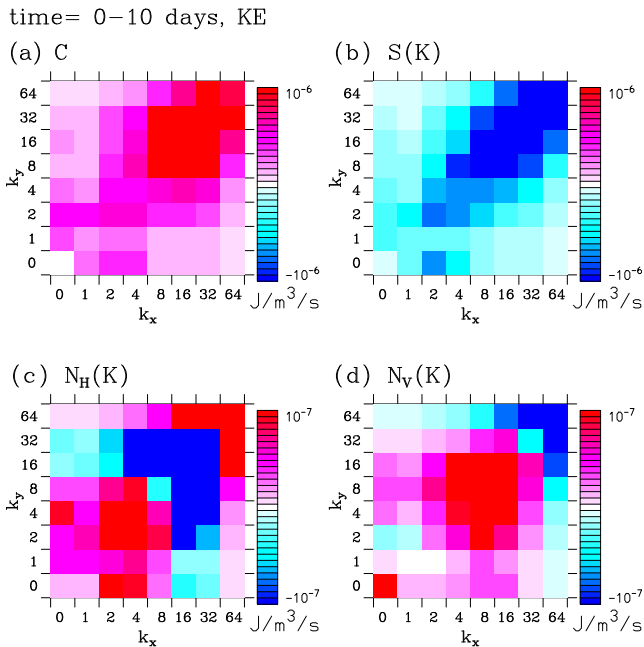


Figure 10. The kinetic energy (KE) budget averaged over the first 10 days ($t = 0–10$ days): the conversion term, \tilde{C} (a), the source term, $\tilde{S}(K)$ (b), the horizontal advection, $\tilde{N}_H(K)$ (c) and the vertical advection, $\tilde{N}_V(K)$ (d). Note the change of color scale between (a–d).

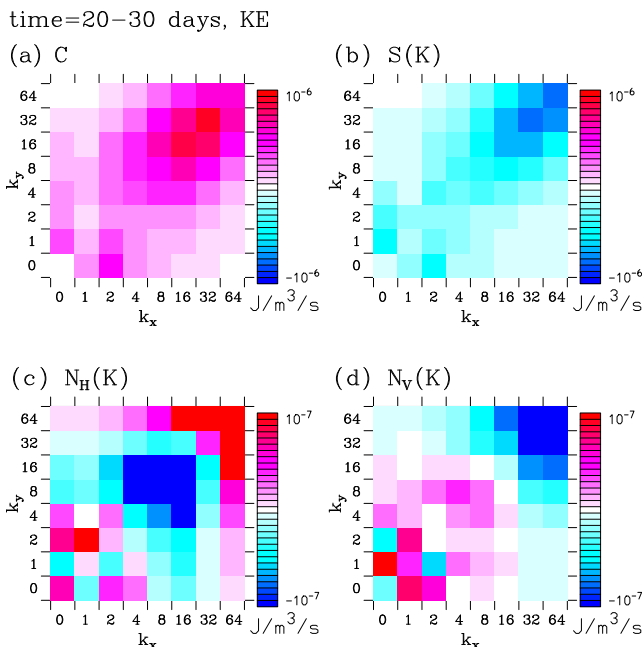


Figure 11. The same as Figure 10 but for the period of $t = 20–30$ days.

Yet, when the analysis is focused on more limited vertical extents, more complex structures emerge in the nonlinear advection terms, i.e., $N_H(K)$ and $N_V(K)$, as already suggested by Figure 9 of Sun et al. (2017). Figure 12 shows the nonlinear horizontal (a, c) and vertical (b, d) advection terms of the kinetic energy for the lower (0–6 km: a, b) and upper (6–12 km: c, d) half of the troposphere, separately. Comparison of (a) and (c) shows that the forward transfer of the kinetic energy from middle scales is only going on in the lower troposphere, and the nonlinear energy transfer by the horizontal advection is mostly upscale in the upper troposphere. The contrast of the vertical advection terms between the upper and lower troposphere is more dramatic (b, d): the terms are overall negative and positive in the lower and upper troposphere, respectively. It means that nonlinear vertical advection overall transports the energy from the lower to the upper troposphere.

6.2. Available Potential Energy (APE)

The potential–energy budget averaged over the first 10 days ($t = 0–10$ days) is shown in Figure 13. The potential energy generated, $\tilde{S}(P)$ (Figure 13a), by diabatic heating and parameterized eddy transports is converted, \tilde{C} (Figures 10a and 13b), into kinetic energy. This energy generation and conversion is strongest for the higher wavenumbers ($k_x \geq 8$ and $k_y \geq 8$), where the conversion somewhat exceeds the generation. Over the lower wavenumbers $k_x \leq 8$ and $k_y \leq 8$ the conversion is somewhat smaller than the generation. An overall balance is thus obtained through a transfer of potential energy from the lower to the higher wavenumbers by nonlinear advection, $\tilde{N}(P)$. The nonlinear tendencies, $\tilde{N}_H(P)$ and $\tilde{N}_V(P)$, due to the horizontal and vertical advection (Figures 13c and 13d), are more or less opposite in signs to the corresponding transfers of kinetic energy: the horizontal advection transfers energy toward the medium scales and the vertical advection transfers it toward higher wavenumbers. For the case of the potential energy, however, vertical advection dominates, and it is mostly responsible for the forward cascade that is required for the balance.

The absolute size of the nonlinear vertical advection term, $\tilde{N}_V(P)$, for APE may particularly be noted: it is about an order of magnitude larger than the nonlinear advection of KE (cf., Figures 10 and 13). This is remarkable, especially considering the fact that the magnitude of APE (Figure 9) is much smaller compared to that of KE (Figure 6). We believe that it reflects the important role of the stable stratification in the present system.

The budget tendencies over the first 10 days do exhibit substantial fluctuations on shorter time–scales, particularly for the generation term, $\tilde{S}(P)$, and the vertical–advection tendency, $\tilde{N}_V(P)$. For example, over the period of $t = 6–8$ days (Figure 14), signs within the budget are reversed compared to the longer–term mean, with potential energy being destroyed rather than generated (i.e., $\tilde{S}(P) < 0$) at the larger scales of $1 \leq k_x \leq 16$ and $4 \leq k_y \leq 16$. A balance is nonetheless maintained with the necessary compensation arising through the vertical advection transferring APE from the highest wavenumbers to lower wavenumbers (i.e., an inverse cascade). As time progresses in the simulation, this mode with an inverse cascade gradually becomes more dominant, and after 20 days, the same behavior is found even under the 10–day averaging, as shown by Figure 15. Notably, at the later stage, potential energy is lost through the negative source term, $\tilde{S}(P) < 0$, at scales over $k_x = 4–16$ or $k_y = 4–16$: thus, the diabatic heating is negatively correlated with virtual potential temperature anomalies at these scales.

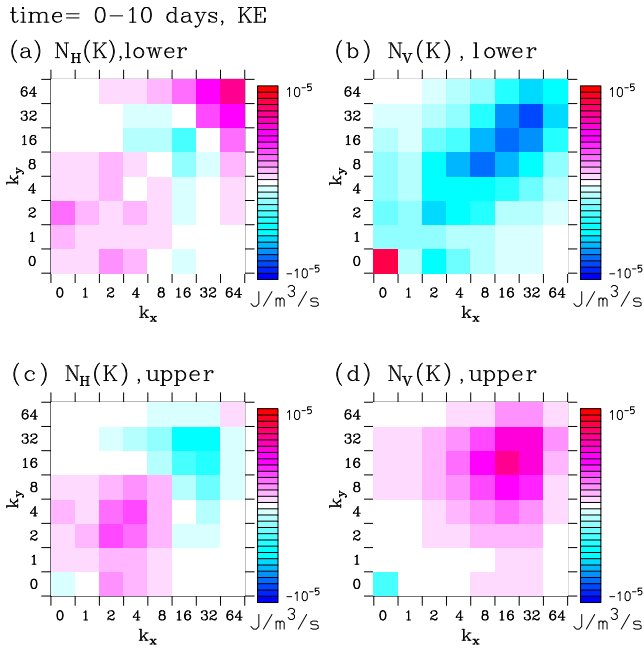


Figure 12. The same as Figure 10 but for the nonlinear horizontal (a, c) and vertical (b) advection terms for the lower (0–6 km; a, b) and upper (6–12 km; c, d) half of the troposphere.

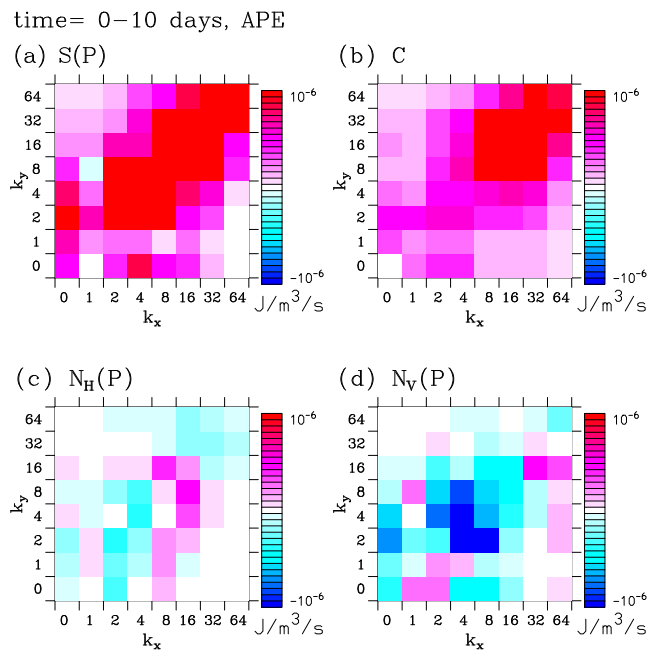


Figure 13. The available potential–energy (APE) budget averaged over the first 10 days ($t = 0–10$ days): the source, $\tilde{S}(P)$ (a), the conversion, \tilde{C} (b), the horizontal advection, $\tilde{N}_H(P)$ (c) and the vertical advection, $\tilde{N}_V(P)$ (d).

The energy cycle identified by the mean wavelet spectrum analysis at the equilibrium state is summarized in Figure 16. Here, we only intend to present an overall picture, and for example, the role of the middle scales is not explicitly indicated; the large and small scales roughly correspond to $k_x = k_y = 1–8$, and $k_x = k_y = 16–64$, respectively, but with precise ranges that change between TKE and APE as well as the periods in concern.

7. Energy Cycle in Sub–Wavelet Space

7.1. Energy Cycle of Precipitation Pulse–Extracted Modes

To analyze the energy cycle in more depth, attempts were made to construct an energy cycle focussed on the leading pulse modes within the precipitation field. However, it turns out that the wavelet modes comprising the first pulse mode of the precipitation field contain little kinetic energy. Other energy variables extracted through the same procedure were not dominant in the overall energy cycle, either. This result is at least partially explained by the fact that a relatively small fraction of the total variance of precipitation can be attributed to an individual pulse component. It further suggests that the leading pulse modes of precipitation, despite being a highly visible manifestation of the organization, are not in themselves especially energetic.

Instead, we focus our attention on those wavelet modes that dominate the potential–energy generation as well as its conversion into the kinetic energy in order to study these key processes in more detail. To this end, we divide the wavelet space into two sub–spaces, based on the process–based decomposition method described in Section 3.4.

7.2. Sub–Wavelet Space With Significant Potential Energy Conversion: Decomposition Into the Buoyant and Nonbuoyant Components

As described in Section 3.4, a system can be decomposed into two components in wavelet space based on a process–based criterion. Here, more specifically, the dominant wavelet modes are defined with a threshold of the standard deviation (Equation 14) after vertical averaging. The vertical averaging allows for the possibility that one of the two variables in concern responds to the other with a vertical shift. Here, we take the energy conversion rate, \tilde{C} , to be the reference variable (i.e., corresponding to χ in Equations 12–14), and separate the full system into buoyant (i.e., $\tilde{\varphi}_1^b$) and nonbuoyant (i.e., $\tilde{\varphi}_1^f$) components.

Figure 17 shows the average over the first 10 days for $\partial \tilde{K}/\partial t$, \tilde{K} , $\tilde{N}(K)$, and $\tilde{S}(K)$ extracted for the modes with a significant energy conversion rate, \tilde{C} (to be termed “buoyant component” for convenience). The kinetic energy associated with the buoyant component, obtained by taking the sum in Equation 43 only over those modes belonging to the buoyant component as defined by Equation 12, tends to increase over these initial 10 days (Figure 17a). Note however, that afterward this tendency weakens, and turns negative over the last 10 days of the simulation. The kinetic–energy spectrum (Figure 17b) is shifted noticeably to lower wavenumbers compared to the full spectrum (cf., Figure 6). This is in spite of the fact that the conversion term, \tilde{C} , is more significant at the higher wavenumbers, as seen in Figures 10 and 11.

The increment rate, $\partial \tilde{K}/\partial t$, (Figure 17a) is significant. Taken together with the overall close balance of the kinetic energy budget discussed in Section 6, this point suggests a recycling time scale less than 10^5 s \sim 1 day, i.e., that the buoyant component is highly transient, and that there are rapid transformations of this component to the nonbuoyant component: i.e., that which is

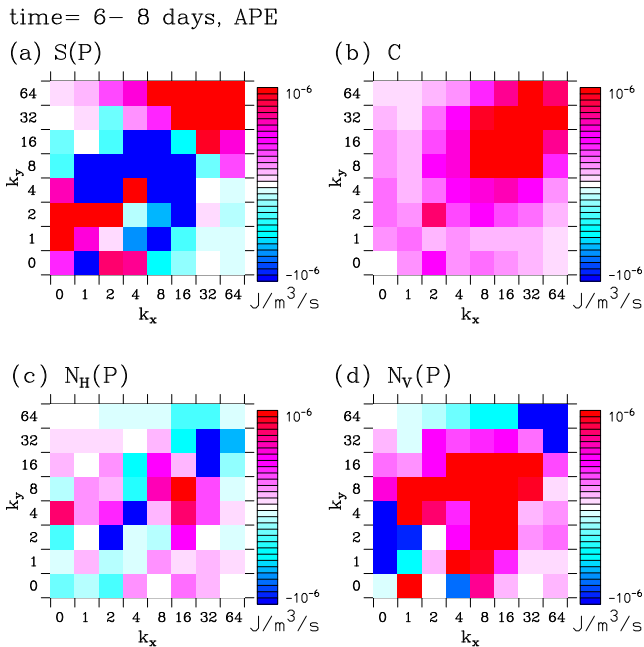


Figure 14. The same as Figure 13, but for the period of $t = 6-8$ days.

7.3. Sub-Wavelet Space With Significant Potential Energy Source: Decomposition Into the Diabatic and Nondiabatic Components

We now turn to the available potential energy (APE) and decompose it into two components based on a criterion of whether a given wavelet mode is significantly generated by diabatic heating: i.e., setting $\chi = \tilde{S}(P)$. This procedure leads to a decomposition of the full system into diabatic and nondiabatic components.

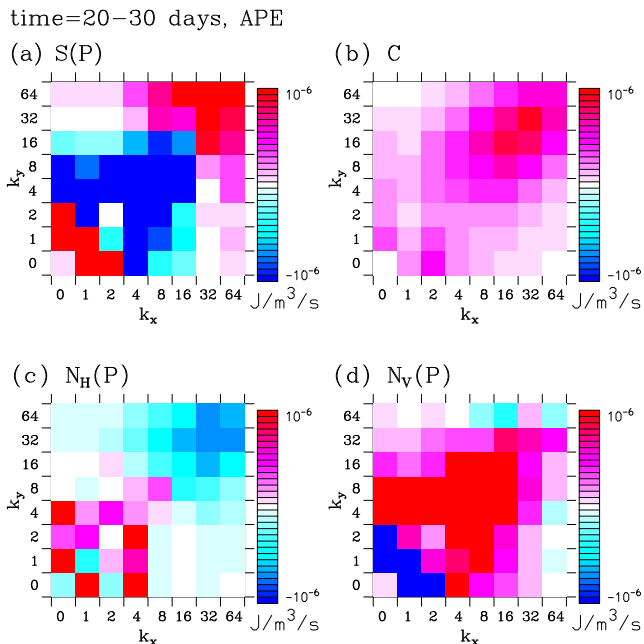


Figure 15. The same as Figure 13, but for the period of $t = 20-30$ days.

not significantly associated with the conversion, \tilde{C} , of the potential energy by buoyancy. At the higher wavenumbers, the energy converted from potential to kinetic energy is rapidly transferred into neighboring nonbuoyant wavelet modes through the pressure term, $\tilde{F}(K)$. Although this term is not explicitly shown here, and only of the order of $10^{-8} \text{ J/m}^3/\text{s}$, this weak transfer rate is sufficient to lose the energy locally within wavenumber space almost immediately. As a result, the kinetic energy at the higher wavenumbers is mostly associated with the nonbuoyant component, as shown by Figure 18.

Figure 18 is the same as Figure 17, but the extractions are for the modes with no significant energy conversion, \tilde{C} (nonbuoyant component). As already remarked, the nonbuoyant component of the kinetic energy is dominant at high wavenumbers, say, above $k_x = k_y = 8$ (Figure 18b), as a result of an immediate conversion from the buoyant component. The nonbuoyant kinetic energy decays slowly with time (Figure 18a), suggesting that a part of this component constitutes a “dead” remnant of a rapidly generated buoyant component. The nonbuoyant kinetic energy is transferred from the nonbuoyant component at medium wavenumbers ($k_x = 8-32$ and $k_y = 8-32$) through the term, $\tilde{N}(K)$, both to lower and higher wavenumbers (Figure 18c).

The identified exchange of the kinetic energy between the buoyant and nonbuoyant components is summarized in Figure 19.

Figure 20 follows the same layout as Figure 17 but for the APE budget based on the extraction of the modes with a significant diabatic–heating source, $\tilde{S}(P)$. First note that the overall magnitude of $\partial \tilde{P}/\partial t$ (Figure 20a) is $10^{-10} \text{ J/m}^3/\text{s}$, i.e., $10^{-4} \text{ J/m}^3/\text{day}$: APE is recycled with a rate of about 10 days. Remarkably, significant contributions of both the increment tendency and the actual APE (Figure 20b) are confined to low wavenumbers ($k_x \leq 4$ and $k_y \leq 4$), although the dominant diabatic heating, $\tilde{S}(P)$, is found at higher wavenumbers (cf., Figure 13). This suggests that the APE generated at the higher wavenumbers must be immediately converted into kinetic energy, as suggested by the spectral distribution of the conversion term, \tilde{C} (Figure 20d). Here, recall the approximate balance, $\tilde{C} \approx \tilde{S}(P) + \tilde{N}(P)$.

The significant APE at the higher wavenumbers ($k_x \geq 8$ and $k_y \geq 8$) is predominantly associated with the nondiabatic wavelet components (those without significant $\tilde{S}(P)$: not shown). This part of the APE is partially maintained by the nonlinear energy transfer, $\tilde{N}(P)$, to those scales from the diabatic modes (Figure 20c). An inspection of Figure 13d further suggests that this nonlinear transfer originates from its vertical component.

As described in Section 6, after 10 days of the simulation, the potential energy source, $\tilde{S}(P)$, becomes negative at larger scales (cf., Figure 15a). As a compensation, energy must be transported from the smaller scales through nonlinear advection, $\tilde{N}(P)$, (Figures 15b and 15c) also reversing its sign from the initial phase. This change of sign is manifest through the diabatic modes

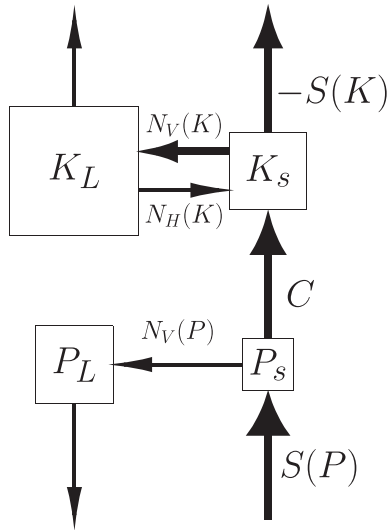


Figure 16. Summary of the energy cycle identified by the mean wavelet–spectrum analysis at the equilibrium state. The potential (lower row) and kinetic (upper row) energies, P and K , in the spectral space are qualitatively divided into large and small scales designated, respectively, by the subscripts, L and s in the left and right columns. The box size of each energy component suggests its relative value, and the principal energy flows are indicated by the arrows, with the arrow sizes qualitatively suggesting the magnitudes of the given transfer processes.

(not shown). The nondiabatic component of potential energy still dominates the smaller scales during this time, and is maintained through a weaker conversion into kinetic energy in compensation.

The same analysis has been repeated by extracting wavelet modes according to those parts of the diabatic heating, $\tilde{S}(P)$, that arise due to cloud microphysics and vertical transports from convection and the boundary–layer processes, $\tilde{S}_c(P)$. These contributions to the diabatic heating were obtained from the tendencies due to individual parameterizations in the model. Strikingly similar results are obtained from extracting modes according to $\tilde{S}_c(P)$ as for the total diabatic heating, $\tilde{S}(P)$. To a slightly lesser extent, the same conclusion also follows from extracting modes according to the potential energy source, $\tilde{S}_R(P)$, from radiative heating (both by shortwave and longwave). Thus, it may be concluded that the condensative and radiative heating play a similar role within the energy cycle.

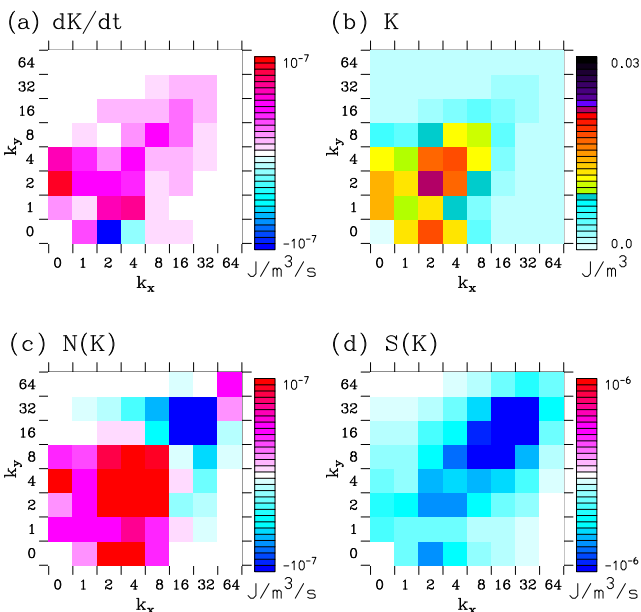
7.4. Nonlinear Energy Transfer by the Nonbuoyant Component

The most important finding from the energy–cycle analysis under the process–based decomposition in the last two subsections is that the nonbuoyant component of the kinetic energy (i.e., the component that is not directly generated by buoyancy forcing) is responsible for a substantial part of the inverse energy cascade, which further feeds some of the energy back to the buoyant component at larger scales, as shown in Figures 17 and 18, and summarized in Figure 19.

In this subsection, to obtain further insights on this nonlinear energy transfer process, we examine a decomposition of the contributions to the nonlinear term. First, we can decompose a given variable into two components by setting, e.g.,

$$\mathbf{v} = \sum_{n=1,2} \mathbf{v}_n,$$

time= 0–10 days, KE, Buoyant Component



where the subscripts $n = 1$ and 2 , respectively, stand for buoyant and nonbuoyant components. As a result, any nonlinear transfer can be decomposed in wavelet space as, e.g.,

$$\tilde{N}_{l,H}(K) = \sum_{n=1,2} \tilde{N}_{l,H,n}(K),$$

where

$$\tilde{N}_{l,H,n}(K) = \tilde{N}_{l,H,n,s}(K) + \tilde{N}_{l,H,n,m}(K) + \tilde{N}_{l,H,n,p}(K),$$

and the last subscript for the terms on the right–hand side, s , m , and p stands for the self–, mixed–, and projected–interactions. These are defined by:

$$\begin{aligned} \tilde{N}_{l,H,n,s}(K) &= -\frac{1}{2}[(\tilde{\rho}\tilde{\mathbf{v}})_{l,n} \cdot \langle \mathbf{u}_n \cdot \nabla_H \mathbf{v}_n \rangle_l + \langle \nabla_H \cdot \rho \mathbf{u}_n \mathbf{v}_n \rangle_l \cdot \tilde{\mathbf{v}}_{l,n}], \\ \tilde{N}_{l,H,n,m}(K) &= -\frac{1}{2}[(\tilde{\rho}\tilde{\mathbf{v}})_{l,n} \cdot \langle \mathbf{u}_n \cdot \nabla_H \mathbf{v}_n \rangle_l + \langle \nabla_H \cdot \rho \mathbf{u}_n \mathbf{v}_n \rangle_l \cdot \tilde{\mathbf{v}}_{l,n}] \\ &\quad -\frac{1}{2}[(\tilde{\rho}\tilde{\mathbf{v}})_{l,n} \cdot \langle \mathbf{u}_n \cdot \nabla_H \mathbf{v}_n \rangle_l + \langle \nabla_H \cdot \rho \mathbf{u}_n \mathbf{v}_n \rangle_l \cdot \tilde{\mathbf{v}}_{l,n}], \\ \tilde{N}_{l,H,n,p}(K) &= -\frac{1}{2}[(\tilde{\rho}\tilde{\mathbf{v}})_{l,n} \cdot \langle \mathbf{u}_n \cdot \nabla_H \mathbf{v}_n \rangle_l + \langle \nabla_H \cdot \rho \mathbf{u}_n \mathbf{v}_n \rangle_l \cdot \tilde{\mathbf{v}}_{l,n}], \end{aligned}$$

Figure 17. The contributions to $\partial \tilde{K} / \partial t$ (a), \tilde{K} (b), $\tilde{N}(K)$ (c), and $\tilde{S}(K)$ (d) extracted for the buoyant component (i.e., the wavelet modes dominant in the energy conversion \tilde{C}). The results are averaged over the first 10 days. Note the change of color scale between (a, c, d).

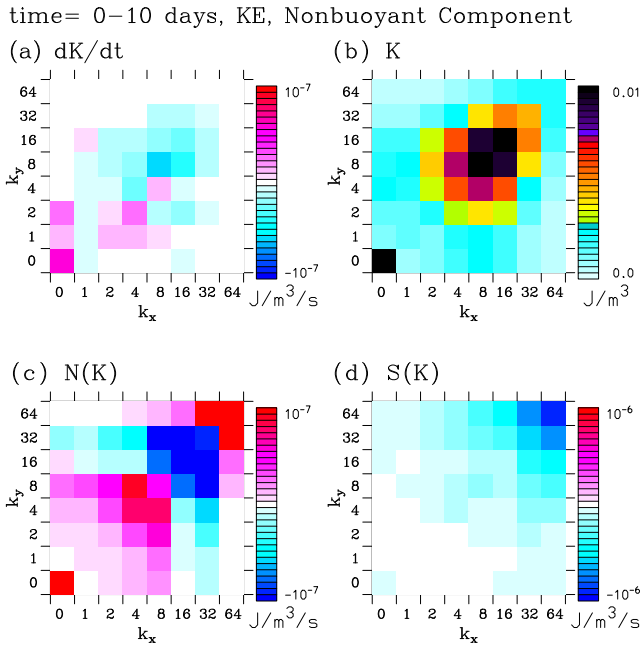


Figure 18. The same as Figure 17 but for the nonbuoyant component (i.e., the wavelet modes that do not dominate the energy conversion \tilde{C}). Note the change of color scale between Figures 17b and 18b.

where $n' (\neq n)$ is another component in concern. For short, we designate this decomposition as:

$$\tilde{N}_n(K) = \tilde{N}_{n,s}(K) + \tilde{N}_{n,m}(K) + \tilde{N}_{n,p}(K), \quad (45)$$

$$\tilde{N}_n(P) = \tilde{N}_{n,s}(P) + \tilde{N}_{n,m}(P) + \tilde{N}_{n,p}(P). \quad (46)$$

The spectra for $\tilde{N}_{n,s}(K)$ (a, c) and $\tilde{N}_{n,m}(K)$ (b, d) are shown in Figure 21 for the buoyant ($n = 1$, (a) and (b)) and nonbuoyant ($n = 2$, (c) and (d)) components. The self-interaction $\tilde{N}_{2,s}(K)$ (c) is mostly responsible for the loss of the nonbuoyant kinetic energy. The gain of the kinetic energy for the nonbuoyant component at the larger scales is, on the other hand, due to the nonlinear interactions with the buoyant component, $\tilde{N}_{2,m}(K)$, and to a lesser extent, due to the projection from the buoyant component through $\tilde{N}_{2,p}(K)$. Here, although the projection terms are not explicitly shown, they can be inferred from comparing Figures 18c, 21c, and 21d by means of Equation 45.

A further separation into horizontal and vertical advectons (not shown) reveals some further details of the full nonlinear transfer process. The nonlinear self-interaction associated with horizontal advection acts to transfer the nonbuoyant kinetic energy to smaller scales, while the self-interaction associated with vertical advection acts to transfer kinetic energy to both larger and smaller scales as well as upwards to the sponge layer.

7.5. Physical-Space Structures of the Buoyant and Nonbuoyant Components

For further insight into the nature of the buoyant and nonbuoyant components of the kinetic energy, as decomposed from the strength of the potential-energy conversion, \tilde{C} , we now examine these components in physical space after inverting the wavelet-space decomposition.

As an initial analysis, we investigated the characteristic vertical structure associated with the buoyant component, which we might expect physically to represent moist convection itself. On choosing any reference height and then

constructing a composite of each velocity component, and of the virtual potential temperature, we consistently found sharp profiles with significant contributions confined to a narrow vertical range around the reference height. Such vertical profiles can be interpreted as a reflection of a highly transient evolution of the convective system in the vertical direction, as schematically suggested in Figure 9b of Arakawa (2004). Crudely speaking, this picture is consistent with the perspective that atmospheric convection consists of a series of thermals as speculated earlier by Scorer and Ludlam (1953), although we do not expect that the present simulation produces the thermals in a realistic manner. Based on this result, we decided to investigate horizontal structure using an analysis level that was chosen rather arbitrarily to be at $z = 8$ km.

From a physical consideration, the nonbuoyant component without significant energy conversion should be interpreted as a type of free wave, which evolves without converting energy from potential to kinetic or vice versa. In the present simulation, the only suitable wave type available is the gravity wave. Thus, we expect that the significant kinetic energy found at the higher wave numbers and associated with the nonbuoyant component (Figure 17b) consists of gravity waves. Since the nonbuoyant component is larger than the buoyant component of kinetic energy, it also follows that most of the kinetic energy found at smaller scales, which may be conventionally called the “convective scale,” consists of gravity waves rather than the convection itself.

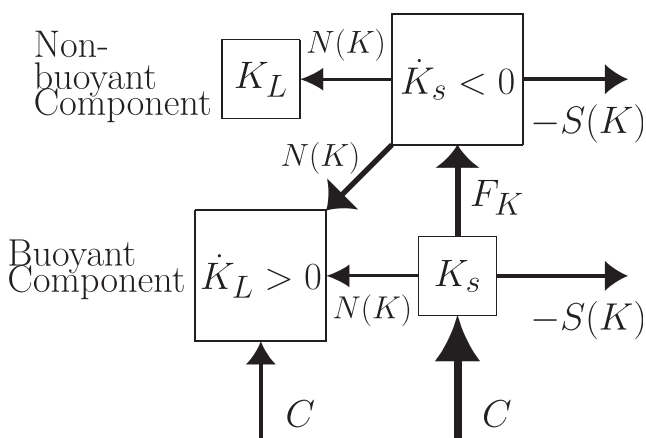


Figure 19. Summary of the identified exchange of kinetic energy between the buoyant and nonbuoyant components, respectively, in the lower and upper rows. Both components are further divided into large and small scales designated, respectively, by the subscripts, L and s in the left and right columns. The box size of each energy component suggests its relative value, and the principal energy flows are indicated by the arrows, with the arrow sizes qualitatively suggesting the magnitudes of the given transfer processes. The temporal tendencies of significant components are also indicated.

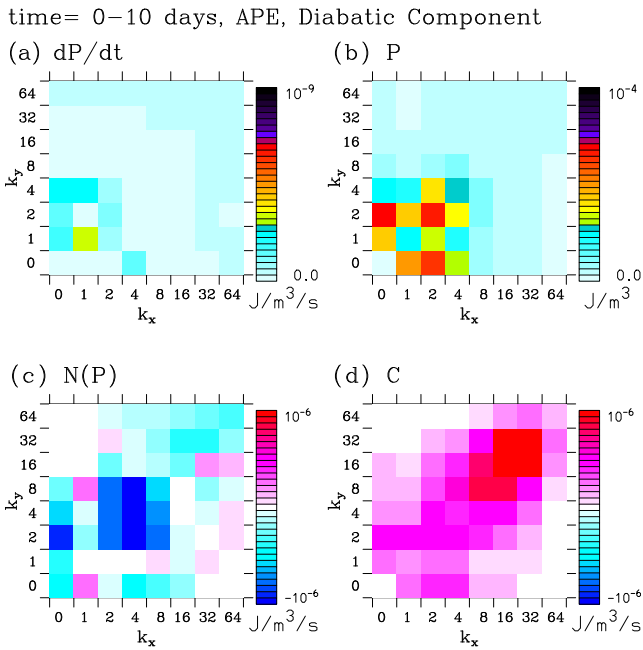


Figure 20. The contributions to $\partial \tilde{P}/\partial t$ (a), \tilde{P} (b), $\tilde{N}(P)$ (c), \tilde{C} (d) extracted for the diabolic component (i.e., the wavelet modes dominant in the diabolic forcing $\tilde{S}(P)$). The results are averaged over the first 10 days. Note the change of color scale between (a, c, d).

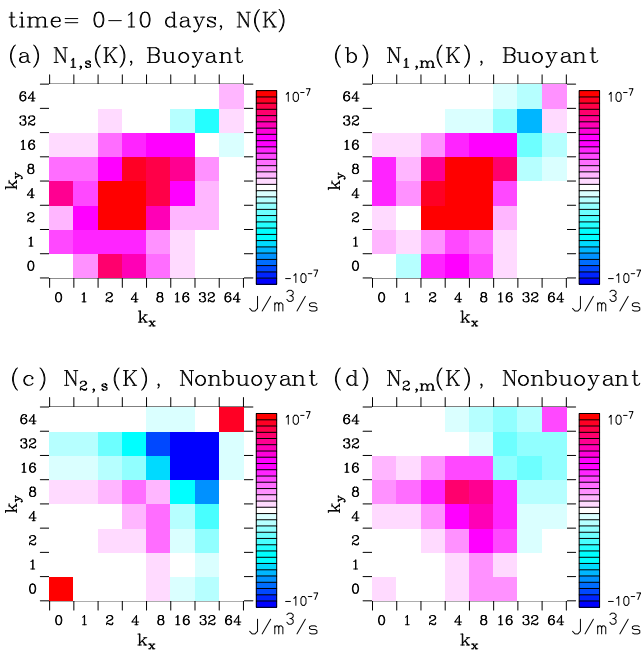


Figure 21. The spectrum of the decomposed nonlinear kinetic energy transfers for the self- ($\tilde{N}_{n,s}(K)$: (a, c)) and mixed- ($\tilde{N}_{n,m}(K)$: (b, d)) interactions of the buoyant ($n = 1$, (a, b)) and nonbuoyant ($n = 2$, (c, d)) components.

However, we should keep in mind that the gravity waves identified here are fully nonlinear, and thus they include both waves and turbulence which would be considered separately in some studies (e.g., Finnigan, 1988; Finnigan & Einaudi, 1981). It may seem counterintuitive to associate gravity waves with a “nonbuoyant” component, but keep in mind that the analysis here identifies propagating waves without significant energy conversion, rather than a direct source for the initiation of gravity waves.

At the initial phase (at $t = 19$ hours: Figure 22), gravity waves are emitted from almost every convective tower, and the comparison of the buoyant (a, b) and nonbuoyant (c, d) components suggests that indeed the latter mostly consists of gravity waves. Radiation of gravity waves gradually becomes less prominent with the evolution of the system. Nevertheless, the concentric ring structures suggesting gravity-wave radiation remain prominent in horizontal sections of the nonbuoyant component even at a later stage. Note also that the updrafts associated with the convective centers are well captured as the buoyant component, although the energy of this component is concentrated toward lower wavenumbers: this reflects a simple fact that, after spatial averaging, a very localized high-amplitude feature need not necessarily contribute significantly to the total power.

Another example of gravity-wave radiation is presented in Figure 23 during the break-down phase of the initial convective cluster formed at $t = 8$ days. In this snapshot, we can identify three gravity waves radiating from convective centers in the lower right quadrant of the domain. It may even be speculated that these wave radiations may induce the break down of the initial convective cluster.

Finally, to demonstrate these horizontal patterns seen in the nonbuoyant component as gravity waves more affirmatively, we plot the vertical velocity, w , and the virtual potential temperature, θ_v , of the nonbuoyant component together at a particular y position along the x -axis for both cases shown in Figures 22 and 23 in Figures 24a and 24b, respectively. Here, the sections are chosen to go through one of the centers of the gravity wave radiations found at around $x = 360$ km and 250 km, respectively. It is seen that the two fields are overall off phase, although the generated waves are clearly not monotonic, reflecting the nonlinear nature of the waves, and fail to show any simple phase relation expected from a monotonic wave.

Although we take these examples from the transient phrase of the simulation, we reiterate that gravity wave radiation patterns persist throughout. When the convective cluster has reached an equilibrium state, the gravity waves are still radiated out from the center of the cluster.

8. Cold-Pool Dynamics

The analysis of the previous section for the kinetic energy was based on a decomposition into those wavelet modes actively involved with the conversion of potential into kinetic energy (the buoyant component) and those not actively involved (the nonbuoyant component). More precisely, this process-based decomposition (cf., Section 3.4) adopted the potential-energy conversion, \tilde{C} , averaged over the troposphere depth, as the reference variable χ in Equations 12–14.

In this section, we turn our attention to the boundary layer, following the same approach, and consider the role of the cold pools. Cold pools have long been proposed as a major mechanism for triggering new convection, initially on the

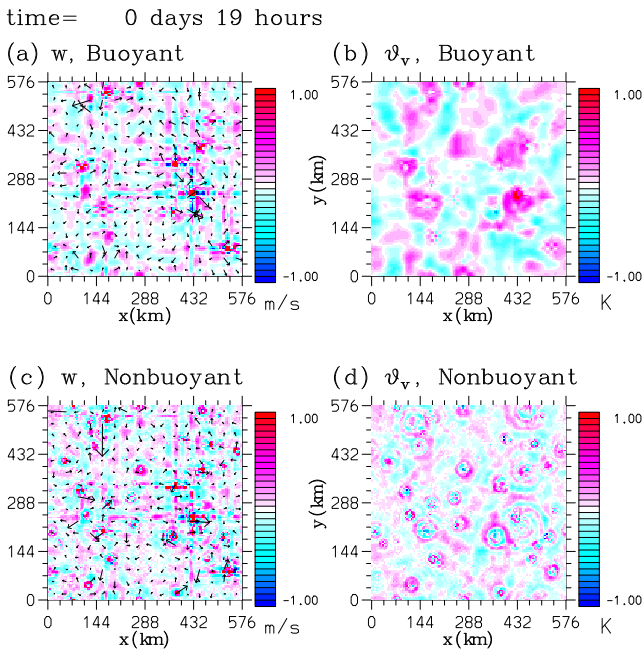


Figure 22. The physical-space structures of the buoyant (a, b) and nonbuoyant (c, d) components of kinetic energy at 8-km height and $t = 19$ hours. (a, c) show the vertical velocity field (shaded) and the horizontal wind vectors (with 1/16 of the length of the sides of the domain corresponding to 2 m/s). (b), (d) show the virtual potential temperature anomaly.

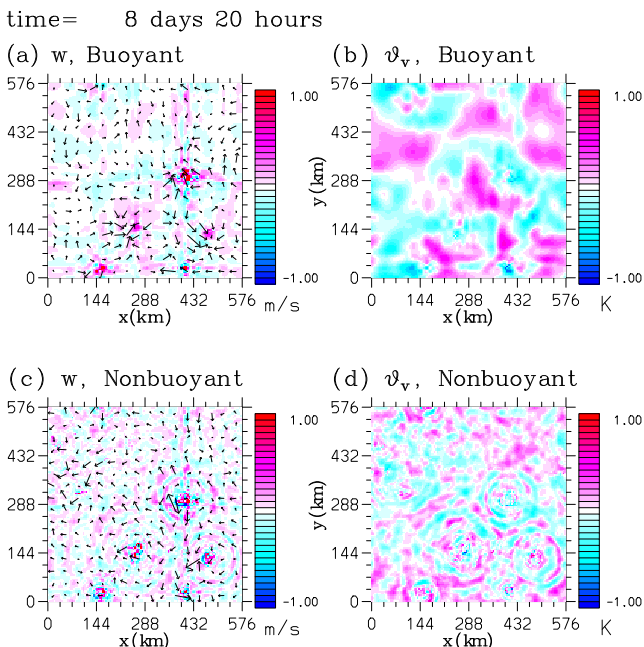


Figure 23. As in Figure 22, but at $t = 8$ days, 20 hr.

basis of various phenomenological observations. Tompkins (2001b) reviews those earlier studies, and presents a detailed analysis of cold-pool dynamics in a cloud-resolving simulation. We also refer to Yano and Ouchtar (2017) for more critical perspectives with further references. The focus here is exclusively on the role of cold pools, as associated with negative-buoyancy anomalies, within the kinetic-energy budget.

The reference variable used is the average of the potential-energy conversion rate, \bar{C} , over the first 1 km of the model. This provides a decomposition into buoyant and nonbuoyant components within the boundary layer, with cold pools being categorized into the buoyant component, since they convert potential into kinetic energy in association with downdrafts, and the formation of near-surface regions of negative buoyancy. On the other hand, the nonbuoyant component within the boundary layer consists mainly of the ripples of gravity waves, which are not of much in concern in the following.

Recall that kinetic energy is generated in physical space by the term, $\theta'_v w$, as seen in Equation 27. Thus, kinetic energy will be generated by a negatively-buoyant cold pool in association with a downdraft, and by a positively-buoyant anomaly with an updraft: energetically speaking, it is not possible for a cold pool to *directly* enhance an updraft.

Two prominent cold-pool events are examined for illustrating the developments of the convective system, which would typically be interpreted as triggers of new convective elements by the cold pools. The following analysis, from a point of view of the energy cycle, emphasizes different points. The cold pools are commonly expected to be maintained by cooling due to the evaporation of precipitating rain. Unfortunately, the rain re-evaporation rate is not directly available in the output. Thus, for examining this effect, it is estimated by a simple formula:

$$\frac{1}{\tau} \frac{q_v^* - q_v}{q_v^*}$$

with a time constant $\tau = 10^4$ s, but capping the estimate so that estimation does not consume more than the available rain water over a time step of $\Delta t = 30$ sec. This formula is derived by Yano and Buniol (2010) as an approximation from an exact formula.

The first event (Figures 25 and 26), shown through a sequence of vertical cross sections of the virtual potential-temperature perturbation, θ'_v , and the evaporative cooling is for the period of $t = 7$ days, 13–16 hr for the buoyant component. A cold pool is generated by a downdraft over $x = 126$ –144 km, just to the east of a convective cloud, as seen in the top frame of Figure 25. The top frame of Figure 26 shows that the evaporative cooling, that generates this cold pool, extends deep beyond 2-km height. Yet, above the top of the well-mixed layer, this cooling tendency is overcompensated by the condensative heating associated with cloud growth as well as adiabatic heating by the downdraft itself. Thus, the cold pool is confined to a shallow layer below 500 m height.

As the cold pool intensifies and propagates gradually westwards, the existing convective cloud dissipates and a new convective tower is triggered on the western edge of the cold pool, at $x = 72$ –81 km on the bottom frame of Figure 25. Here, in the literature, a positively-buoyant anomaly generated at the top head of cold pool is attributed to an *action* of the cold pool itself, yet,

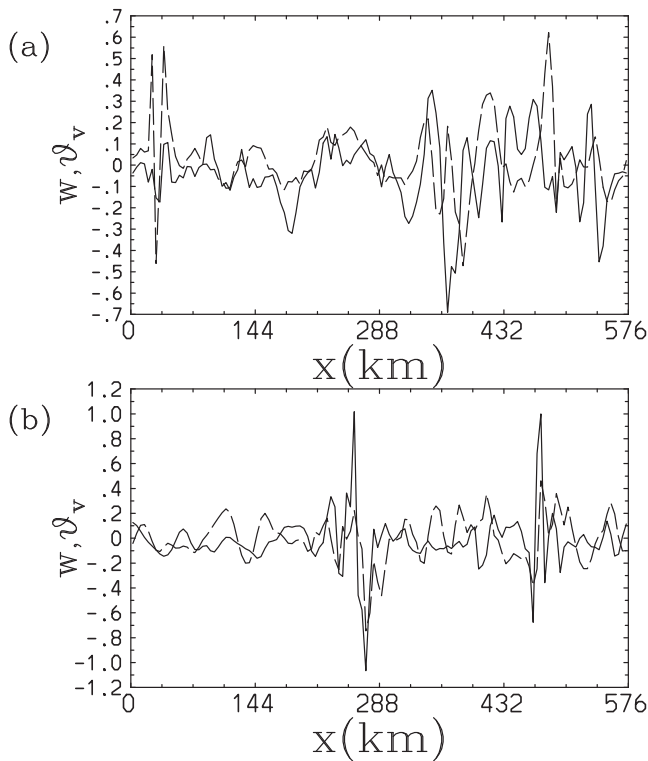


Figure 24. Plot of the vertical velocity, w (solid), and the virtual potential temperature, θ_v (dashed), of the nonbuoyant component at a particular y position along the x -axis: (a) with $y = 175$ km and (b) 144 km for the cases shown in Figures 22 and 23, respectively.

without specifying an associated physical process. This anomaly is more likely a consequence of adiabatic heating by a dry downdraft aloft, as the figure suggests. The updraft resulting from this positively-buoyant anomaly further leads to condensative heating, as suggested by growing clouds.

From an energetic point of view, it is not possible for a cold pool, associated with a negative buoyancy, to generate an updraft. As seen in the middle two frames of Figure 25, the cold pool rather drives a narrow downdraft immediately adjacent to this updraft to the west, in association with the evaporative cooling of rain, as seen in Figure 26. Moreover, as the updraft further grows, the cold pool weakens as a consequence, as seen in the bottom frame.

The second event for the period of $t = 7$ days, 19–21 hr may be more dramatic, as shown in Figure 27 for the sections of the virtual potential-temperature perturbation, θ'_v . Over the region of $x = 36$ –72 km, a cold pool is generated by a downdraft underneath a convective cloud, as seen in the top frame, presumably as a consequence of associated evaporative cooling. In this manner, a very mild downdraft identified over $x = 9$ –36 km seen in the first two frames is much enhanced over the cold pool ($x = 36$ –54 km) in the last two frames. This positive feedback process leads to an eastward wind burst along the cold pool, which flows into a buoyant layer just east, with the burst developing an upward motion. The enhancing upward motion, in turn, enhances pre-existing convection over $x = 144$ –180 km.

9. Discussions

9.1. Energy Transfer Process in the Wavelet Space

The purpose of the present study has been to infer the generation mechanism of convective organization as seen in the precipitation field by examining the energy cycle in wavelet space. The main finding is that both kinetic and potential energies tend to be transferred upscale by nonlinear advection processes. This tendency, which may be loosely referred to as the “inverse cascade,” is reminiscent of the one found in two-dimensional turbulence.

This analogy is partially supported by the fact that the bulk of the nonlinear transfer of kinetic energy is due to horizontal advection. However, the analogy should not be pushed too far: most importantly, the nonlinear transfer of potential energy (APE) is mostly due to vertical advection. The nonlinear horizontal advection, moreover, does not simply transfer kinetic energy upscale in the present system; rather it is the kinetic energy of the medium scales ($k_x = 8$ –32 and $k_y = 8$ –32) that is transferred toward the other scales. However, the energy transfer by horizontal advection toward the smallest scales is over-compensated by the energy-transfer tendency to the larger scales due to vertical advection from the same scales. Thus, the combination of horizontal- and vertical-advection tendencies is important for the overall upscale cascade to be realized.

The overall tendency for an inverse cascade found here is much closer to the original speculation by Lilly (1983) than later findings by Lindborg (1999, 2007) and Deusebio et al. (2014) of a forward cascade in stratified atmospheric turbulence, and as also demonstrated for an idealized stratified turbulence simulation without rotation effect by Lindborg (2006). It may also be worthwhile to note that Lilly (1983) emphasizes an important role of the gravity-wave modes in his analysis. Nevertheless, the cascade elucidated in the present study is more involved than a simple inverse cascade, suggesting a glimpse of rich morphologies of the turbulence cascade processes that have been gradually revealed over the years, as reviewed by Alexakis and Biferale (2018).

The importance of vertical advection for nonlinear energy transfer in this system may not appear intuitive from the perspective of standard homogeneous turbulence theories, either two- or three-dimensional. However, the well-mixed, horizontally-homogeneous convective boundary layer in the absence of vertical wind shear (cf., Part II of Yano, 2023) may serve as a good analogue. Under this situation, the domain-averaged vertical flux becomes a key quantity controlling the evolution of both the kinetic and potential energies, with an absence of horizontal

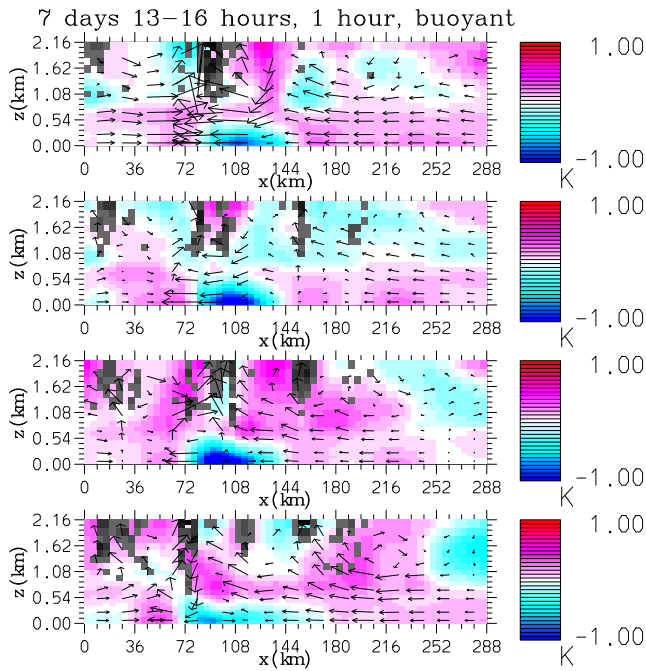


Figure 25. A sequence of vertical sections averaged over $y = 432\text{--}504$ km for the lowest 2.1 km, beginning at $t = 7$ days, 13 hr in the upper panel and progressing forwards in time in subsequent panels at 1-hr intervals. Each section shows the buoyancy component of the virtual potential-temperature perturbation, θ'_v , defined as a deviation from the horizontal-domain average. Also shown with gray shading are the clouds, as defined by a total-condensate mixing ratio above 0.02 g/kg, and wind vectors of the x - and z -components. Only the left half of the domain is shown, and only the buoyant wavelet component is considered, associated with a significant energy conversion rate, \tilde{C} , below 1 km.

Thus, we recover the so-called free-ride balance (Fraedrich & McBride, 1989), or alternatively known as the weak-temperature gradient (WTG) approximation (Sobel et al., 2001). This conclusion is noteworthy, because the free ride (WTG) is typically considered as a large-scale balance in the tropical atmosphere. The present analysis suggests that it can further be extended toward the convective scale.

An unexpected feature in the later stages of the simulation is that APE is no longer generated at the larger scales ($k_x \leq 16$ and $k_y \leq 16$) by diabatic heating, but rather mostly lost, except at the very largest scales ($k_x + k_y \leq 4$). To maintain an equilibrium, APE must be transported to those scales by nonlinear advection. As seen in Figure 15d, this process is mostly handled by the vertical advection. However, this does not reflect a true inverse cascade because the nonlinear vertical advection term is negative at the largest scales ($k_x + k_y \leq 4$), where diabatic-generation of APE is still found. We may yet notice a true inverse cascade in the horizontal advection term (Figure 15c) with APE lost the scales of $k_x \geq 8$ and $k_y \geq 8$ and gained at the larger scales, but to a lesser extent. As a whole, in the later equilibrium stage of the convective organization in this simulation, the idea suggested by Yang (2019) that APE tends to be accumulated on the large scale does not appear to explain the aggregation process.

9.3. Gravity-Wave Dynamics

Convection generates gravity waves and the convective scale is full of gravity wave motions. There are already extensive linear-dynamics studies to elucidate the generation process of gravity waves from convection (e.g., Bretherton & Smolarkiewicz, 1989). Mapes (1993) further speculates that these gravity waves work as a trigger for subsequent convective events. Uccellini and Koch (1987) compare multiple observational studies on convection-gravity wave interactions, and a good example case study can be found in Morcrette et al. (2006) and Marsham and Parker (2006), studied from an observational and modeling perspective respectively.

transport by assumption. In particular, the nonlinear eddy heat transport maintains an observed vertical homogeneity of potential temperature over the boundary layer. In contrast, the tendency toward homogenization in the present system is in the horizontal direction.

9.2. Potential-Energy Budget and the Free-Ride Principle

It is important to emphasize that the tendency found in the cycle of the potential energy (APE) is no way steady: the direction of the energy cascade changes over time rather frequently. In particular, over the first 10 days, APE is overall transferred to smaller scales by nonlinear advection (cf., Figure 13). This fact is significant, because it is during this same period that the spectrum of potential energy steadily moves to the larger scales. Hence, this tendency cannot be explained by a nonlinear advection process, but is due to a slight imbalance between the diabatic energy generation, $\tilde{S}(P)$, and its conversion, \tilde{C} , into kinetic energy. This initial tendency of APE accumulating on the large scale may be considered a major process leading to the convective organization, as suggested by Yang (2019).

After about 6 days of simulation, APE as a whole begins to diminish to a much smaller value (cf., Figure 9). However, generation of APE at the smaller scales ($k_x \geq 32$ or $k_y \geq 32$) does not diminish to the same extent (cf., Figure 14a): the APE generated by diabatic heating at those scales is effectively converted into kinetic energy almost immediately by the conversion term \tilde{C} (cf., Figure 14b). Setting the right-hand side of Equation 23 to zero, and using the definitions in Equations 26 and 27, we find that this process corresponds to the approximate relation

$$w \frac{d\tilde{\theta}_v}{dz} \simeq Q.$$

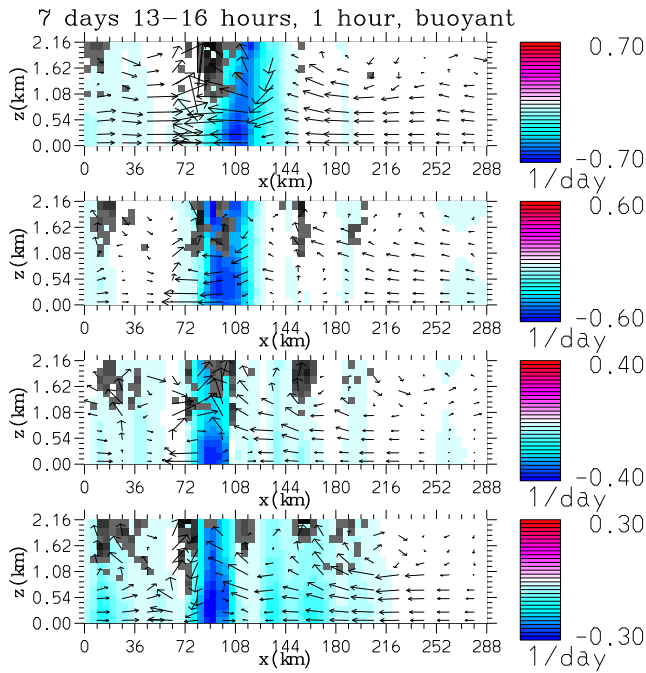


Figure 26. The same as Figure 25, but the shades are the estimated re- evaporation rate (in the unit of moisture tendency: 1/day) with a negative sign for a cooling.

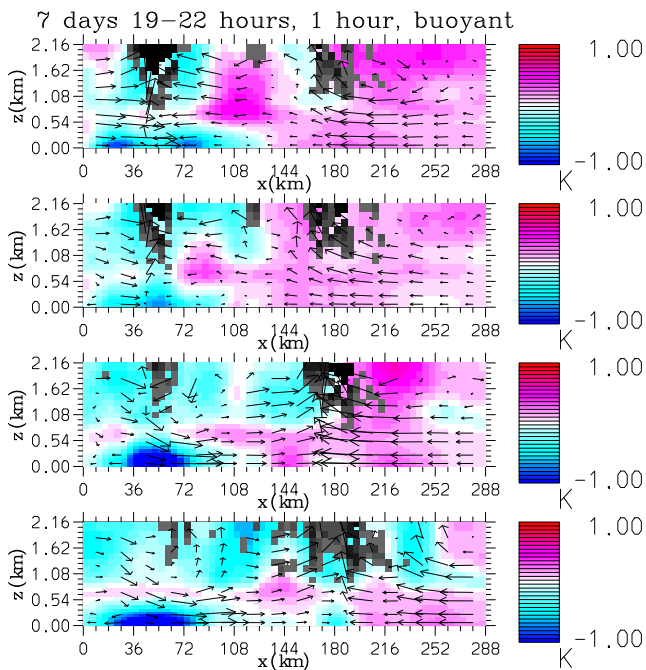


Figure 27. The same section as for Figure 25, but a sequence beginning at $t = 7$ days, 19 hr, and with a one-hour interval.

The main originality of the present work is to show quantitatively that the majority of the kinetic energy at the convective scale, defined by the wave- numbers, say, larger than $k = 16$ (less than 36 km in wavelength), consists of gravity waves, as seen in Figure 18b. Here, the gravity waves have been identified from those wavelet modes of the kinetic energy that are not significantly generated by the potential–energy conversion, \tilde{C} . The results of the wavelet decomposition are interpreted in the sense that the buoyancy forcing, \tilde{C} , generates the convective kinetic energy, and that this is immediately converted by the pressure conversion term, $\tilde{F}(K)$, into gravity wave motions that radiate from the convective centers.

Whether these gravity waves contribute to the triggering of new convective centers is a difficult question to answer affirmatively under the energy–cycle analysis adopted here. The convective kinetic energy at the convective scales is weak compared to that associated with the gravity waves, and thus, a slight conversion of the gravity–wave energy back to convection does not show up in the bulk energy–cycle analysis.

However, the present study does reveal a more curious aspect of these gravity–wave dynamics: the associated kinetic energy is transferred to larger scales through the nonlinear energy-transfer term, $\tilde{N}(K)$, due to their self-advection (Figure 18c). We have further shown that this upscale energy cascade by nonlinear interactions of the gravity waves is the main mechanism for organizing the kinetic energy onto the large scales, that further drives the convective organization. The importance of advective nonlinearity of gravity waves was already suggested by Hines (1991) in interpreting stratospheric gravity–wave spectra. However, this aspect has not been investigated much.

Some simple linear theories (e.g., Nicholls et al., 1991; Pandya et al., 1993) suggest that as gravity waves propagate away from convection, an area of homogeneous descent also spreads outwards from the convective center. In the present framework of analysis, the homogeneous descent would be categorized into the buoyant component; i.e., being actively supported by the conversion of potential energy through the buoyancy-generation term of Equation 27. Unfortunately, due to the hourly sampling rate of the output, and given that a single convective element rarely lasts more than 1 hour, it has not been possible to verify directly in a visual manner the process of the descent area spreading as the gravity waves propagate outwards. Nevertheless, such a gradual spread of the descent area may constitute a basic elementary process for the inverse energy cascade.

Yang (2021) further proposes that gravity waves more directly contribute to the formation of convective organization by their linear resonance with convection. That study clearly shares a common view with the present study by emphasizing an important role of gravity waves in convective organization. Yet, a major difference of the present study is in pointing out that the nonlinear nature of the gravity–wave dynamics contributes to convective organization.

One way to interpret the transfer of energy to larger scales through the nonlinear self–interactions of gravity waves may be as a homogenization tendency of the environment by the gravity waves. A good analogy may be the vertical mixing through stirring across an interface with a discontinuity in density, as studied by laboratory experiments, and reviewed in Ch. 9 of Turner (1973) and Ch. 13 of Yano (2023). A similar mixing process can also be induced by a shear instability at a discontinuous interface (e.g., Thorpe, 1971). In the latter case, a perturbation generated by the instability presents a regular

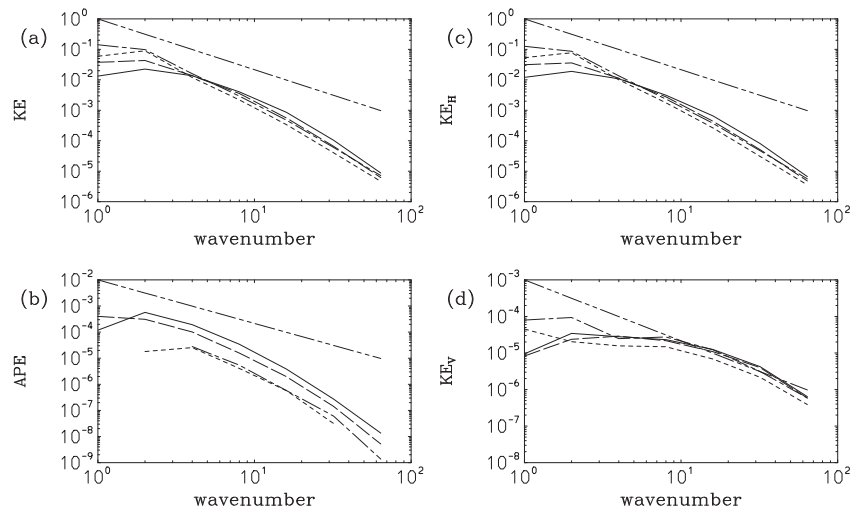


Figure 28. The power spectra of the (a) kinetic and (b) potential energies. The spectra of kinetic energy are further plotted for the (c) horizontal and (d) vertical components, separately. The slope for $-5/3$ power law is also plotted as a double-chain dashed curve on each frame. Spectra are for every 10 days from the end of the day 1 with varying types of the curves.

wave structure, which amplifies with time by keeping a well-defined single wavenumber. The only major difference is that the generated wave disturbance keeps growing in situ, whereas it propagates away from the instability source in the present system.

9.4. Power Spectra

It would be natural to ask what kind of power laws the energy spectra follow. Unfortunately, the resolution and domain size of the present simulation are not well separated enough to obtain spectra over a wide wavenumber range. The largest wavenumber available is $k = 64$, and thus spectra can be evaluated only slightly above one decade, which is insufficient to establish a clear slope. Nevertheless, some tentative remarks may be offered.

The total kinetic-energy spectra appear slightly steeper than a $-5/3$ power law for scales above around wavenumber three, and are relatively flat at the smallest wavenumbers (Figure 28a). The corresponding spectra for APE are shown in Figure 28b: they are not far from a $-5/3$ power law, although noticeably steeper. Spectra for the horizontal components of kinetic energy (Figure 28c) are essentially reproductions of the total spectra over much of the range, reflecting the domination of the total kinetic energy by the horizontal components. The contribution from the vertical component is less than 1% at the largest scales (Figure 28d). However, at the highest wavenumbers, the two contributions become comparable, with the slope of the vertical kinetic-energy spectra being much gentler than that of the horizontal components.

9.5. Limits of the Present Study

9.5.1. Numerical Limits

Various limitations of the present study may be remarked. Most obviously, the domain size is rather small with sizes of length 576 km with a relatively crude horizontal resolution of 4 km. It would be much desirable to repeat a similar simulation with a much larger domain with a higher horizontal resolution, thus the tendency of convection to be organized into the larger scales can be investigated with a full resolution.

Less evident, yet potentially a more serious issue is the relatively small number of vertical levels (70) adopted in the study. Note that the actual analysis is limited to the lowest 12 km, and up to this level only 56 levels are available with the spacing of the vertical levels increasing to about 700 m at 12 km height. It is known that low vertical resolution can impact the energy spectra and cascade in simulations of dry stratified turbulence. Especially, Bartello (2000) shows that a spurious inverse cascade can develop when excessive vertical eddy viscosity is specified to compensate low vertical resolution. Billant and Chomaz (2001) point out from their theoretical

analysis that the characteristic vertical scale of a strongly-stratified system is given by $U/\sigma^{1/2}$, where U is the characteristic velocity, and $\sigma^{1/2}$ is the Brunt–Väisälä frequency (cf., Equation 26). Waite (2016) supports this theoretical prediction via his numerical simulations. This scale is about $U/\sigma^{1/2} \simeq 500$ m in the present simulation, assuming that $U \simeq 5$ m/s and $\sigma^{1/2} \simeq 10^{-2}$ s⁻¹.

Clearly it is a numerically very challenging to satisfy all those requirements. At the same time, need for fully resolving stratified turbulence for a simulation of convective organization is not quite obvious, because operational models appear to work well without satisfying such a stringent requirement for the vertical resolution. See: Lindzen and Fox–Rabinovits (1989), Cullen (2017), and Skamarock et al. (2019) for relevant discussions.

9.5.2. Need for Further Analyses

Rich morphologies of convective organization revealed by the present study in wavelet space are hardly over-emphasized. Yet, the present study has managed to present only a glimpse of those rich morphologies. For example, only short remarks were offered on the vertical dependence of the nonlinear energy transfer processes in association with Figure 12.

The advantage of the wavelet method has been clearly exploited in successfully extracting the gravity–wave modes away from the isolated convective towers. However, the full strength of the wavelet method is yet to fully exploited. Especially, its capacity of efficiently extracting spatially isolated structures (pulse extraction, Section 3.5) is not much exploited in the present study. In principle, it should be possible to trace the transfer of the energy from one wavelet mode to another in association with, for example, initiation of convection, by identifying it as a key wavelet mode. Yet, the required procedure turns out to be rather tedious with many analysis steps, that can be performed only manually. To perform such an analysis effectively, more frequent output of data than presently available is much desirable, too.

Another rather unsatisfactory aspect of the work is not separating out the nonlinear advection terms into the inter-mode energy transfers and the vertical fluxes. The procedure is less obvious under the wavelet decomposition with lack of a simple rule for expressing a single wavelet mode in terms of products of the other wavelet modes, as is the case with the Fourier decomposition. Probably, this is the technically most challenging issue to be resolved.

9.6. Concluding Remarks and Perspectives

The energy cycle of a convectively organized system has been examined in wavelet space. A clear tendency for kinetic energy to be transferred to larger scales by nonlinear advection has particularly been elucidated. Importantly, this inverse cascade is realized through interplays between horizontal and vertical advection processes. Perhaps the most surprising result in the authors' point of view is that the kinetic energy generated by buoyancy forcing at the small scales is mostly immediately converted into gravity waves. The nonlinear self-interactions of these gravity waves, in turn, are mostly responsible for the inverse cascade process. This is in contrast to, for example, the estimation of Lilly (1983) that only a small fraction of energy generated at the convective scale participates in the inverse cascade.

Here, the gravity–wave modes have been identified as those wavelet modes of the kinetic energy that are not significantly generated by the potential–energy conversion, \tilde{C} , taking advantage of the fact that a wavelet decomposition can efficiently extract modes that are localized in space. By construction the localized convective modes do not *mix* with those gravity-wave modes under a wavelet decomposition (cf., Yano, Bechtold, et al., 2004; Yano, Moncrieff, & Wu, 2001), as would happen with solely scale dependent decompositions.

In the equilibrium state, the available potential energy is lost by diabatic heating at the large scales ($k_x \leq 16$ and $k_y \leq 16$), apart from the very largest scales of $k_x + k_y \leq 2$. Vertical advection drives the nonlinear energy transfer from those largest scales to smaller scales. The overall picture of the convective organization process identified by the present study is schematically summarized in Figure 29. As a whole, the present study has attained insight into the convection dynamics associated with an organized precipitation system. A circulation is organized onto the large scale, as elucidated by the kinetic-energy budget, and we believe this to be responsible for driving the precipitation field also into an organized large-scale configuration.

Yet, we still need to distinguish between these two organization processes carefully. The organization of the circulation onto the large scale is established relatively early in the simulation, over first few days (Figure 6), and

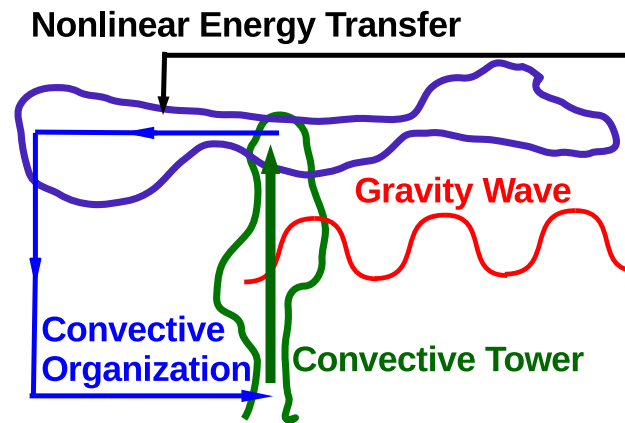


Figure 29. A schematic to summarize the convective organization process identified by the present study: the kinetic energy generated by condensative heating in association with the individual convective elements, shown as a convective tower in green here, is immediately transformed into gravity wave motions, indicated by red. The latter induces an upscale nonlinear energy transfer to a domain scale, as suggested by the black arrow, leading to a convective organization, schematically suggested by a “stratiform cloud” with dark blue, which is associated with a large-scale circulation suggested by the arrow in light blue.

the kinetic-energy spectrum is thereafter near to an equilibrium (Figure 7). On the other hand, the generation of precipitation organization takes much longer (cf., Figure 1). An initial organization of the precipitation is manifest on day 8 but breaks down in only 24 hr, and it takes a further 10 days for the precipitation organization to be fully established as an equilibrium state. Thus, the question of the precipitation organization must be addressed separately from that of the circulation: the energy cycle between the potential (APE) and kinetic (KE) energies does not directly address the question of the more *immediate* mechanism of generating precipitation organization. To a certain extent, the latter is ultimately a consequence of cloud microphysical processes. A basic strategy to address this question could be to perform a budget analysis of the precipitation and related fields in wavelet space in an analogous manner to the energy-cycle analysis considered here. It is obvious that it amounts to another work to perform, which is left for future study.

Data Availability Statement

Data used for the present study is available through CEDA: <https://catalogue.ceda.ac.uk/uuid/6c93ff856bda41d99342702593ec6053>.

References

- Alexakis, A., & Biferale, L. (2018). Cascade and transitions in turbulence flows. *Physics Reports*, 769–769, 1–101.
- Arakawa, A. (2004). The cumulus parameterization problem: Past, present, and future. *Journal of Climate*, 17(13), 2493–2525. [https://doi.org/10.1175/1520-0442\(2004\)017<2493:ratcpp>2.0.co;2](https://doi.org/10.1175/1520-0442(2004)017<2493:ratcpp>2.0.co;2)
- Augier, P., & Lindborg, E. (2013). A new formulation of the spectrum energy budget of the atmosphere, with application to two high-resolution general circulation models. *Journal of the Atmospheric Sciences*, 70(7), 2293–2308. <https://doi.org/10.1175/jas-d-12-0281.1>
- Bartello, P. (2000). Potential vorticity, resonance and dissipation in rotating convective turbulence. In R. H. Kerr, P. Fox, & C.-H. Moeng (Eds.), *Geophysical and Astrophysical Convection* (pp. 309–321).
- Billant, P., & Chomaz, J.-M. (2001). Self-similarity of strongly stratified flows. *Physics of Fluids*, 13(6), 1645–1651. <https://doi.org/10.1063/1.1369125>
- Bretherton, C. S., Blossey, P. N., & Khairoutdinov, M. (2005). An energy-balance analysis of deep convective self-aggregation above uniform SST. *Journal of the Atmospheric Sciences*, 62(12), 4273–4292. <https://doi.org/10.1175/jas3614.1>
- Bretherton, C. S., & Smolarkiewicz, P. K. (1989). Gravity waves, compensating subsidence and detrainment around cumulus clouds. *Journal of the Atmospheric Sciences*, 46(6), 740–759. [https://doi.org/10.1175/1520-0469\(1989\)046<0740:gwsad>2.0.co;2](https://doi.org/10.1175/1520-0469(1989)046<0740:gwsad>2.0.co;2)
- Charney, J. G., & Eliassen, A. (1964). On the growth of the hurricane depression. *Journal of the Atmospheric Sciences*, 21(1), 68–75. [https://doi.org/10.1175/1520-0469\(1964\)021<0068:otgoth>2.0.co;2](https://doi.org/10.1175/1520-0469(1964)021<0068:otgoth>2.0.co;2)
- Cho, J. Y.-K., & Polvani, L. M. (1996). The emergence of jets and vortices in freely evolving, shallow-water turbulence on a sphere. *Physics of Fluids*, 8(6), 1531–1552. <https://doi.org/10.1063/1.868929>
- Cullen, M. J. P. (2017). The impact of high vertical resolution in the Met Office Unified Model. *Quarterly Journal of the Royal Meteorological Society*, 143(702), 278–287. <https://doi.org/10.1002/qj.2920>

Acknowledgments

JYY thanks Chris Holloway for discussions as well as arranging the model data. This work has been much facilitated by a support of the Royal Society International Exchange program (IES/R1/180099), that enabled JYY’s multiple visits to the University of Reading. The authors also much appreciate positive and supportive, yet critical reviews by the three reviewers.

- Davies, T., Cullen, M. J. P., Malcolm, A. J., Mawson, M. H., Staniforth, A., White, A. A., & Wood, N. (2005). A new dynamical core for the Met Office's global and regional modelling of the atmosphere. *Quarterly Journal of the Royal Meteorological Society*, *131*(608), 1759–1782. <https://doi.org/10.1256/qj.04.101>
- Deusebio, E., Augier, P., & Lindborg, E. (2014). Third-order structure functions in rotating and stratified turbulence: A comparison between numerical, analytical and observational results. *Journal of Fluid Mechanics*, *755*, 294–313. <https://doi.org/10.1017/jfm.2014.414>
- Emanuel, K. A. (1987). An air–sea interaction model of intraseasonal oscillations in the tropics. *Journal of the Atmospheric Sciences*, *44*(16), 2324–2340. [https://doi.org/10.1175/1520-0469\(1987\)044<2324:aaismo>2.0.co;2](https://doi.org/10.1175/1520-0469(1987)044<2324:aaismo>2.0.co;2)
- Finnigan, J. J. (1988). Kinetic energy transfer between internal gravity waves and turbulence. *Journal of the Atmospheric Sciences*, *45*(3), 486–505. [https://doi.org/10.1175/1520-0469\(1988\)045<0486:ketbig>2.0.co;2](https://doi.org/10.1175/1520-0469(1988)045<0486:ketbig>2.0.co;2)
- Finnigan, J. J., & Einaudi, F. (1981). The interaction between an internal gravity wave and the planetary boundary layer. Part II: Effect of the wave on the turbulence structure. *Quarterly Journal of the Royal Meteorological Society*, *107*(454), 807–832. <https://doi.org/10.1002/qj.49710745405>
- Fournier, A. (2002). Atmospheric energetics in the wavelet domain. Part I: Governing equations and interpretation for idealized flows. *Journal of the Atmospheric Sciences*, *59*(7), 1182–1197. [https://doi.org/10.1175/1520-0469\(2002\)059<1182:aetwd>2.0.co;2](https://doi.org/10.1175/1520-0469(2002)059<1182:aetwd>2.0.co;2)
- Fournier, A. (2003). Atmospheric energetics in the wavelet domain. Part II: Time-averaged observed atmospheric blocking. *Journal of the Atmospheric Sciences*, *60*(2), 319–338. [https://doi.org/10.1175/1520-0469\(2003\)060<0319:aetwd>2.0.co;2](https://doi.org/10.1175/1520-0469(2003)060<0319:aetwd>2.0.co;2)
- Fournier, A. (2005). Instantaneous wavelet energetic transfers between atmospheric blocking and local eddies. *Journal of Climate*, *18*(13), 2151–2171. <https://doi.org/10.1175/jcli3381.1>
- Fraedrich, K., & McBride, J. L. (1989). The physical mechanism of CISK and the free-ride balance. *Journal of the Atmospheric Sciences*, *46*(17), 2642–2648. [https://doi.org/10.1175/1520-0469\(1989\)046<2642:tpmoca>2.0.co;2](https://doi.org/10.1175/1520-0469(1989)046<2642:tpmoca>2.0.co;2)
- Gregory, D., & Rowntree, P. R. (1990). A mass flux convection scheme with representation of cloud ensemble characteristics and stability-dependent closure. *Monthly Weather Review*, *118*(7), 1483–1506. [https://doi.org/10.1175/1520-0493\(1990\)118<1483:amfcsw>2.0.co;2](https://doi.org/10.1175/1520-0493(1990)118<1483:amfcsw>2.0.co;2)
- Hayashi, Y. (1970). A theory of large-scale equatorial waves generated by condensation heat and accelerating the zonal wind. *Journal of the Meteorological Society of Japan*, *48*(2), 140–160. https://doi.org/10.2151/jmsj1965.48.2_140
- Held, I. M., Hemler, R. S., & Ramaswamy, V. (1993). Radiative-convective equilibrium with explicit two-dimensional moist convection. *Journal of the Atmospheric Sciences*, *50*(23), 3909–3927. [https://doi.org/10.1175/1520-0469\(1993\)050<3909:rcewet>2.0.co;2](https://doi.org/10.1175/1520-0469(1993)050<3909:rcewet>2.0.co;2)
- Hines, C. O. (1991). The saturation of gravity waves in the middle atmosphere. Part II: Development of Doppler-spread theory. *Journal of Atmospheric Sciences*, *48*, 1361–1379. [https://doi.org/10.1175/1520-0469\(1991\)048<1361:TSGOW1>2.0.CO;2](https://doi.org/10.1175/1520-0469(1991)048<1361:TSGOW1>2.0.CO;2)
- Holloway, C. E., Wang, A. A., Bony, S., Muller, C., Masunaga, H., L'Ecuyer, T. S., et al. (2017). Observing convective aggregation. *Surveys in Geophysics*, *38*(6), 1199–1236. <https://doi.org/10.1007/s10712-017-9419-1>
- Holloway, C. E., & Woolnough, S. J. (2016). The sensitivity of convective aggregation to diabatic processes in idealized radiative-convective equilibria. *Journal of Advances in Modeling Earth Systems*, *8*(1), 166–195. <https://doi.org/10.1002/2015ms000511>
- Holloway, C. E., Woolnough, S. J., & Lister, G. M. S. (2013). The effects of explicit versus parameterized convection on the MJO in a large-domain high-resolution tropical case study. Part I: Characterization of large-scale organization and propagation. *Journal of the Atmospheric Sciences*, *70*(5), 1342–1369. <https://doi.org/10.1175/jas-d-12-0227.1>
- Houze, R. A., Jr. (2018). 100 years of research on mesoscale convective systems. *Meteorological Monographs*, *59*, 17.1–17.54. <https://doi.org/10.1175/AMSMONOGRAPHIS-D-18-0001.1>
- Houze, R. A., Jr., & Betts, A. K. (1981). Convection in GATE. *Reviews of Geophysics and Space Physics*, *19*(4), 541–576. <https://doi.org/10.1029/rg019i004p00541>
- Kimura, Y., & Herring, J. R. (2012). Energy spectra of stably stratified turbulence. *Journal of Fluid Mechanics*, *698*, 19–50.
- Lai, K. W., & Waite, M. L. (2023). Kinetic energy spectra and spectral budget of radiative-convective equilibrium. *Journal of the Atmospheric Sciences*, *80*(8), 1953–1970. <https://doi.org/10.1175/jas-d-22-0173.1>
- Lean, H. W., Clark, P. A., Dixon, M., Roberts, N. M., Fitch, A., Forbes, R., & Halliwell, C. (2008). Characteristics of high-resolution versions of the Met Office Unified model for forecasting convection over the United Kingdom. *Monthly Weather Review*, *136*(9), 3408–3424. <https://doi.org/10.1175/2008mwr2332.1>
- Lilly, D. K. (1962). On the numerical simulation of buoyant convection. *Tellus*, *14*(2), 148–172. <https://doi.org/10.3402/tellusa.v14i2.9537>
- Lilly, D. K. (1983). Stratified turbulence and the mesoscale variability of the atmosphere. *Journal of the Atmospheric Sciences*, *40*(3), 749–761. [https://doi.org/10.1175/1520-0469\(1983\)040<0749:statmv>2.0.co;2](https://doi.org/10.1175/1520-0469(1983)040<0749:statmv>2.0.co;2)
- Lilly, D. K., Bassett, G., Droegemeier, K., & Bartello, P. (1998). Stratified turbulence in the atmospheric mesoscales. *Theoretical and Computational Fluid Dynamics*, *11*(3–4), 139–153. <https://doi.org/10.1007/s001620050085>
- Lin, H. (2022). The Madden-Julian oscillation. *Atmosphere-Ocean*, *60*(3–4), 338–359. <https://doi.org/10.1080/07055900.2022.2072267>
- Lindborg, E. (1999). Can the atmospheric kinetic energy spectrum be explained by two-dimensional turbulence? *Journal of Fluid Mechanics*, *388*, 259–288. <https://doi.org/10.1017/s0022112099004851>
- Lindborg, E. (2006). The energy cascade in a strongly stratified fluid. *Journal of Fluid Mechanics*, *550*(-1), 207–242. <https://doi.org/10.1017/s0022112005008128>
- Lindborg, E. (2007). Horizontal wavenumber spectra of vertical velocity and horizontal divergence in upper troposphere and lower stratosphere. *Journal of the Atmospheric Sciences*, *64*(3), 1017–1025. <https://doi.org/10.1175/jas3864.1>
- Lindzen, R. S. (1974). Wave-CSIK in the tropics. *Journal of the Atmospheric Sciences*, *31*(1), 156–179. [https://doi.org/10.1175/1520-0469\(1974\)031<0156:wciit>2.0.co;2](https://doi.org/10.1175/1520-0469(1974)031<0156:wciit>2.0.co;2)
- Lindzen, R. S., & Fox-Rabinovits, M. (1989). Consistent vertical and horizontal resolution. *Monthly Weather Review*, *117*(11), 2575–2583. [https://doi.org/10.1175/1520-0493\(1989\)117<2575:cvahr>2.0.co;2](https://doi.org/10.1175/1520-0493(1989)117<2575:cvahr>2.0.co;2)
- Lorenz, E. N. (1955). Available potential energy and the maintenance of the general circulation. *Tellus*, *7*(2), 157–167. <https://doi.org/10.1111/j.2153-3490.1955.tb01148.x>
- Mallat, S. (1998). *A wavelet tour of signal processing* (2nd ed., p. 637). Academic Press.
- Mapes, B. E. (1993). Gregarious tropical convection. *Journal of the Atmospheric Sciences*, *50*(13), 2026–2037. [https://doi.org/10.1175/1520-0469\(1993\)050<2026:gtc>2.0.co;2](https://doi.org/10.1175/1520-0469(1993)050<2026:gtc>2.0.co;2)
- Marshall, J. H., & Parker, D. J. (2006). Secondary initiation of multiple bands of cumulonimbus over southern Britain. Part II: Dynamics of secondary initiation. *Quarterly Journal of the Royal Meteorological Society*, *132*(617), 1053–1072. <https://doi.org/10.1256/qj.05.152>
- Meneveau, C. (1991). Analysis of turbulence in the orthonormal wavelet. *Journal of Fluid Mechanics*, *232*(-1), 469–520. <https://doi.org/10.1017/s0022112091003786>
- Meyer, Y. (1992). *Wavelets and operators* (p. 223). Cambridge University Press.

- Morcrette, C. J., Browning, K. A., Blyth, A. M., Bozier, K. E., Clark, P. A., Ladd, D., et al. (2006). Secondary initiation of multiple bands of cumulonimbus over southern Britain. Part I: An observational case study. *Quarterly Journal of the Royal Meteorological Society*, 132(617), 1021–1051. <https://doi.org/10.1256/qj.05.151>
- Muller, C., Yang, D., Craig, G., Cronin, T., Fildier, B., Haerter, J. O., et al. (2022). Spontaneous aggregation of convective storms. *Annual Review of Fluid Mechanics*, 54(1), 133–157. <https://doi.org/10.1146/annurev-fluid-022421-011319>
- Nakajima, K., & Matsuno, T. (1988). Numerical experiments concerning the origin of cloud clusters in the tropical atmosphere. *Journal of the Meteorological Society of Japan*, 66(2), 309–329. https://doi.org/10.2151/jmsj1965.66.2_309
- Nakazawa, T. (1988). Tropical super clusters within interseasonal variations over the western Pacific. *Journal of the Meteorological Society of Japan*, 66(6), 823–839. https://doi.org/10.2151/jmsj1965.66.6_823
- Neelin, J. D., Held, I. M., & Cook, K. H. (1987). Evaporation-wind feedback and low-frequency variability in the tropical atmosphere. *Journal of the Atmospheric Sciences*, 44(16), 2341–2348. [https://doi.org/10.1175/1520-0469\(1987\)044<2341:ewfalf>2.0.co;2](https://doi.org/10.1175/1520-0469(1987)044<2341:ewfalf>2.0.co;2)
- Nicholls, M. E., Pielke, M. E. R. A., & Cottons, W. R. (1991). Thermally forced gravity waves in an atmosphere at rest. *Journal of the Atmospheric Sciences*, 48(16), 1869–1884. [https://doi.org/10.1175/1520-0469\(1991\)048<1869:tfgwia>2.0.co;2](https://doi.org/10.1175/1520-0469(1991)048<1869:tfgwia>2.0.co;2)
- Oort, A. H. (1964). On the energetics of the mean and eddy circulations in the lower stratosphere. *Tellus*, 16(3), 309–327. <https://doi.org/10.3402/tellusa.v16i3.8978>
- Oort, A. H., & Peixoto, J. P. (1974). The annual cycle of the energetics of the atmosphere on a planetary scale. *Journal of Geophysical Research*, 79(18), 2705–2719. <https://doi.org/10.1029/jc079i018p02705>
- Ooyama, K. V. (1982). Conceptual evolution of the theory and modeling of the tropical cyclone. *Journal of the Meteorological Society of Japan*, 60(1), 369–380. https://doi.org/10.2151/jmsj1965.60.1_369
- Pandya, P., Durren, D., & Bretherton, C. S. (1993). Comments on “thermally forced gravity waves in an atmosphere at rest”. *Journal of the Atmospheric Sciences*, 50(24), 4097–4101. [https://doi.org/10.1175/1520-0469\(1993\)050<4097:cofgwi>2.0.co;2](https://doi.org/10.1175/1520-0469(1993)050<4097:cofgwi>2.0.co;2)
- Riley, J. J., & Lindborg, E. (2008). Stratified turbulence: A possible interpretation of some geophysical turbulence measurements. *Journal of the Atmospheric Sciences*, 65(7), 2416–2424. <https://doi.org/10.1175/2007jas2455.1>
- Saltsman, B. (1957). Equations governing the energetics of the larger scales of atmospheric turbulence in the domain of wave number. *Journal of the Atmospheric Sciences*, 14(6), 513–523. [https://doi.org/10.1175/1520-0469\(1957\)014<0513:egteot>2.0.co;2](https://doi.org/10.1175/1520-0469(1957)014<0513:egteot>2.0.co;2)
- Saltzman, B. (1958). Some hemispheric spectral statistics. *Journal of the Atmospheric Sciences*, 15(3), 259–263. [https://doi.org/10.1175/1520-0469\(1958\)015<0259:shss>2.0.co;2](https://doi.org/10.1175/1520-0469(1958)015<0259:shss>2.0.co;2)
- Scorer, R. S., & Ludlam, F. H. (1953). Bubble theory of penetrative convection. *Quarterly Journal of the Royal Meteorological Society*, 79(339), 94–103. <https://doi.org/10.1002/qj.49707933908>
- Skamarock, W. C., Snyder, C., Klemp, J. B., & Park, S.-H. (2019). Vertical resolution requirements in atmospheric simulation. *Monthly Weather Review*, 147(7), 2641–2656. <https://doi.org/10.1175/mwr-d-19-0043.1>
- Smagorinsky, J. (1963). General circulation experiments with the primitive equations. *Monthly Weather Review*, 91(3), 99–164. [https://doi.org/10.1175/1520-0493\(1963\)091<0099:gcewtp>2.3.co;2](https://doi.org/10.1175/1520-0493(1963)091<0099:gcewtp>2.3.co;2)
- Smith, R. K., & Montgomery, M. T. (2023). *Tropical cyclones* (p. 600). Elsevier.
- Sobel, A. H., Nilsson, J., & Polvani, L. M. (2001). The weak temperature gradient approximation and balanced moisture waves. *Journal of the Atmospheric Sciences*, 58, 3650–3665.
- Su, H., Bretherton, C. S., & Chen, S. S. (2000). Self-aggregation and large-scale control of tropical deep convection: A modeling study. *Journal of the Atmospheric Sciences*, 57(11), 1797–1816. [https://doi.org/10.1175/1520-0469\(2000\)057<1797:saalsc>2.0.co;2](https://doi.org/10.1175/1520-0469(2000)057<1797:saalsc>2.0.co;2)
- Sun, Y. Q., Rotunno, R., & Zhang, F. (2017). Contributions of moist convection and internal gravity waves to building the atmospheric -5/3 kinetic energy spectra. *Journal of the Atmospheric Sciences*, 74(1), 185–201. <https://doi.org/10.1175/jas-d-16-0097.1>
- Tennekes, H. (1978). Turbulent flow in two and three dimensions. *Bulletin American Meteorology Social*, 59(1), 22–28. [https://doi.org/10.1175/1520-0477\(1978\)059<0022:tfitat>2.0.co;2](https://doi.org/10.1175/1520-0477(1978)059<0022:tfitat>2.0.co;2)
- Thorpe, S. A. (1971). Experiments on the instability of stratified shear flows: Miscible fluids. *Journal of Fluid Mechanics*, 46(2), 299–319. <https://doi.org/10.1017/s0022112071000557>
- Tompkins, A. M. (2001a). Organization of tropical convection in low vertical wind shears: The role of water vapor. *Journal of the Atmospheric Sciences*, 58(6), 529–545. [https://doi.org/10.1175/1520-0469\(2001\)058<0529:ootcil>2.0.co;2](https://doi.org/10.1175/1520-0469(2001)058<0529:ootcil>2.0.co;2)
- Tompkins, A. M. (2001b). Organization of tropical convection in low vertical wind shears: The role of cold pools. *Journal of the Atmospheric Sciences*, 58(13), 1650–1672. [https://doi.org/10.1175/1520-0469\(2001\)058<1650:ootcil>2.0.co;2](https://doi.org/10.1175/1520-0469(2001)058<1650:ootcil>2.0.co;2)
- Turner, J. S. (1973). *Buoyancy effects in fluids* (p. 367). Cambridge University Press.
- Uccellini, L. W., & Koch, S. E. (1987). The synoptic setting and possible sources for mesoscale wave disturbances. *Monthly Weather Review*, 115(3), 721–729. [https://doi.org/10.1175/1520-0493\(1987\)115<0721:tssape>2.0.co;2](https://doi.org/10.1175/1520-0493(1987)115<0721:tssape>2.0.co;2)
- Waite, M. L. (2016). Dependence of model energy spectra on vertical resolution. *Monthly Weather Review*, 144(4), 1407–1421. <https://doi.org/10.1175/mwr-d-15-0316.1>
- Wheeler, M., & Kiladis, G. N. (1999). Convectively-coupled equatorial waves: Analysis of clouds and temperature in the wavenumber-frequency domain. *Journal of the Atmospheric Sciences*, 56(3), 374–399. [https://doi.org/10.1175/1520-0469\(1999\)056<0374:ccewao>2.0.co;2](https://doi.org/10.1175/1520-0469(1999)056<0374:ccewao>2.0.co;2)
- Wilson, D. R., & Ballard, S. P. (1999). A microphysically based precipitation scheme for the UK Meteorological Office Unified Model. *Quarterly Journal of the Royal Meteorological Society*, 125(557), 1607–1636. <https://doi.org/10.1002/qj.49712555707>
- Wing, A. A. (2019). Self-aggregation of deep convection and its implications for climate. *Current Climate Change Reports*, 5, 1–11. <https://doi.org/10.1007/s40641-019-00120-3>
- Wing, A. A., Emanuel, K., Holloway, C. E., & Muller, C. (2017). Convective self-aggregation in numerical simulations: A review. *Surveys in Geophysics*, 38(6), 1173–1197. <https://doi.org/10.1007/s10712-017-9408-4>
- Yang, D. (2018). Boundary layer diabatic processes, the virtual effect, and convective self-aggregation. *Journal of Advances in Modeling Earth Systems*, 10(9), 2163–2176. <https://doi.org/10.1029/2017ms001261>
- Yang, D. (2019). Convective heating leads to self-aggregation by generating available potential energy. *Geophysical Research Letters*, 46(17–18), 10687–10696. <https://doi.org/10.1029/2019gl083805>
- Yang, D. (2021). A shallow-water model for convective self-aggregation. *Journal of the Atmospheric Sciences*, 78(2), 571–582. <https://doi.org/10.1175/jas-d-20-0031.1>
- Yano, J.-I. (1998). Planetary-scale coherent structures of tropical moist convection. *Australian Journal of Physics*, 51(5), 865–874. <https://doi.org/10.1071/p97078>
- Yano, J.-I. (2003). The cumulus parameterization problem in the context of MJO simulations. In *Proceedings for the MJO workshop, ECMWF, 2–5 November 2003* (pp. 115–127). Retrieved from <http://www.ecmwf.int/publications/library/do/references/list/17124>
- Yano, J.-I. (2023). *Geophysical convection dynamics* (p. 302pp). Elsevier.

- Yano, J.-I., Bechtold, P., Redelsperger, J.-L., & Guichard, F. (2004). Wavelet-Compressed Representation of deep moist convection. *Monthly Weather Review*, *132*(6), 1472–1486. [https://doi.org/10.1175/1520-0493\(2004\)132<1472:wrodmc>2.0.co;2](https://doi.org/10.1175/1520-0493(2004)132<1472:wrodmc>2.0.co;2)
- Yano, J.-I., Blender, R., Zhang, C., & Fraedrich, K. (2004). $1/f$ noise and pulse-like events in the tropical atmospheric surface variabilities. *Quart. J. Roy. Meteor. Soc.*, *300*(600), 1697–1721. <https://doi.org/10.1256/qj.03.42>
- Yano, J.-I., & Buniol, D. (2010). A minimum bulk microphysics. *Atmospheric Chemistry and Physics Discussions*, *10*, 30305–30345. <https://doi.org/10.5194/acpd-10-30305-2010>
- Yano, J.-I., & Emanuel, K. A. (1991). An improved model of the equatorial troposphere and its coupling with the stratosphere. *Journal of the Atmospheric Sciences*, *48*(3), 377–389. [https://doi.org/10.1175/1520-0469\(1991\)048<0377:aimote>2.0.co;2](https://doi.org/10.1175/1520-0469(1991)048<0377:aimote>2.0.co;2)
- Yano, J.-I., & Jakubiak, B. (2016). Wavelet-based verification of the quantitative precipitation forecast. *Dynamics of Atmospheres and Oceans*, *74*, 14–29. <https://doi.org/10.1016/j.dynatmoce.2016.02.001>
- Yano, J.-I., McWilliams, J. C., & Moncrieff, M. W. (1996). Fractality in idealized simulations of large-scale tropical cloud systems. *Monthly Weather Review*, *124*(5), 838–848. [https://doi.org/10.1175/1520-0493\(1996\)124<0838:fiisol>2.0.co;2](https://doi.org/10.1175/1520-0493(1996)124<0838:fiisol>2.0.co;2)
- Yano, J.-I., McWilliams, J. C., Moncrieff, M. W., & Emanuel, K. A. (1995). Hierarchical tropical cloud systems in an analog shallow water model. *Journal of the Atmospheric Sciences*, *52*(10), 1723–1742. [https://doi.org/10.1175/1520-0469\(1995\)052<1723:hctesia>2.0.co;2](https://doi.org/10.1175/1520-0469(1995)052<1723:hctesia>2.0.co;2)
- Yano, J.-I., Moncrieff, M. W., & Wu, X. (2001). Wavelet analysis of simulated tropical convective cloud systems part II: Decomposition of convective-scale and mesoscale structures. *Journal of the Atmospheric Sciences*, *58*(8), 868–876. [https://doi.org/10.1175/1520-0469\(2001\)058<0868:waostc>2.0.co;2](https://doi.org/10.1175/1520-0469(2001)058<0868:waostc>2.0.co;2)
- Yano, J.-I., Moncrieff, M. W., Wu, X., & Yamada, M. (2001). Wavelet analysis of simulated tropical convective cloud systems part I: Basic analysis. *Journal of the Atmospheric Sciences*, *58*(8), 850–867. [https://doi.org/10.1175/1520-0469\(2001\)058<0850:waostc>2.0.co;2](https://doi.org/10.1175/1520-0469(2001)058<0850:waostc>2.0.co;2)
- Yano, J.-I., & Ouchtar, E. (2017). Convective initiation uncertainties without trigger or stochasticity: Probabilistic description by the Liouville equation and Bayes' theorem. *Quarterly Journal of the Royal Meteorological Society*, *143*(705), 2015–2035. <https://doi.org/10.1002/qj.3064>
- Zhang, C. (2005). Madden-Julian oscillation. *Reviews of Geophysics*, *43*(2), RG2003. <https://doi.org/10.1029/2004RG000158>